

The Nickel Mass Distribution of Stripped-Envelope Supernovae: Implications for Additional Power Sources

NILOUFAR AFSARIARDCHI,¹ MARIA R. DROUT,^{1, 2} DAVID K. KHATAMI,³ CHRISTOPHER D. MATZNER,¹ DAE-SIK MOON,¹ AND YUAN QI NI¹

¹ *David A. Dunlap Department of Astronomy and Astrophysics, University of Toronto,*

50 St. George Street, Toronto, Ontario, M5S 3H4 Canada

² *The Observatories of the Carnegie Institution for Science, 813 Santa Barbara St, Pasadena, CA, 91101, USA*

³ *Department of Astronomy, University of California, Berkeley, CA, 94720*

(Received; Revised; Accepted)

Submitted to ApJ

ABSTRACT

We perform a systematic study of the ^{56}Ni mass (M_{Ni}) of 27 stripped envelope supernovae (SESN) with both well-constrained rise times and late-time coverage (>60 days) by modeling their light-curve tails. Based on this sample, we find that using “Arnett’s rule” with observed peak times (t_{p}) and luminosities (L_{p}) will overestimate M_{Ni} for SESN by a factor of ~ 2 . Recently, Khatami & Kasen (2019) presented a new analytic model relating t_{p} and L_{p} of a radioactive-powered SN to its M_{Ni} that addresses several limitations of Arnett-like models, but depends on a dimensionless parameter β , which is sensitive to details of the progenitor system and explosion mechanism. Using the observed t_{p} , L_{p} , and tail-measured M_{Ni} values for the sample of SESN, we observationally calibrate β for the first time—finding $0.0 < \beta < 1.71$ with a median value of 0.70. Despite scatter, we demonstrate that the model of Khatami & Kasen (2019) coupled with these empirically-calibrated β values yields a significantly improved measurement of M_{Ni} when only photospheric data is available. However, these observationally-constrained β values are systematically lower than those inferred from numerical simulations, due primarily to the observed sample having significantly higher (0.2–0.4 dex) L_{p} for a given M_{Ni} . We investigate this discrepancy and find that while effects due to composition, mixing, and asymmetry can increase L_{p} none can explain the systematically low β values. However, the discrepancy with simulations can be alleviated if ~ 7 –50% of L_{p} for the observed sample comes from sources other than the radioactive decay of ^{56}Ni . Either shock cooling or magnetar spin down could provide the requisite luminosity, with the former requiring that a substantive fraction of SESN undergo late-stage mass loss or envelope inflation. Finally, we find that even with our improved measurements, the M_{Ni} values of SESN are a factor of ~ 3 larger than those of hydrogen-rich Type II SN, indicating that these supernovae are inherently different in terms of their progenitor initial mass distributions or explosion mechanisms.

Keywords: Supernovae: general

1. INTRODUCTION

Stripped Envelope Supernovae (SESN) are core-collapse supernovae (SNe) whose progenitors shed a significant fraction of their H envelope before the explosion (Clocchiatti et al. 1996; Woosley et al. 2002). It is widely thought that the light curves of SESNe are predominantly powered by the radioactive decay of ^{56}Ni synthesized in the explosion (Arnett 1982). In this picture, while shock

cooling emission following the often-undetected shock breakout (SBO) may also contribute to the observed luminosity of SESNe during the first few days post-explosion, the main peak of the bolometric light curve is powered by $^{56}\text{Ni} \rightarrow ^{56}\text{Co}$ radioactive decay. Following the peak, the light curves of SESNe rapidly decline and subsequently enter a phase of linear (magnitude) decay, which is powered by the $^{56}\text{Co} \rightarrow ^{56}\text{Fe}$ chain. This phase typically begins at epochs $\gtrsim 60$ days (Clocchiatti & Wheeler 1997). The resulting shape of the light curve is not only sensitive to the total mass of ^{56}Ni , but also to the total ejecta mass (M_{ej}), the distribution of M_{Ni} within the ejecta, and the degree to which ^{56}Ni deposition is asymmetric (Utrobin et al. 2017).

Corresponding author: Niloufar Afsariardchi
 afsariardchi@astro.utoronto.ca

There exists significant diversity within SESNe. Spectroscopically, they are divided into distinct sub-types: IIb, Ib, Ic, and Ic-BL SNe (See [Filippenko 1997](#), for a review). The first three sub-types are generally thought to be produced by increasingly more stripped progenitors ([Maund 2018](#)). Type IIb SNe have signatures of both H and He lines, although their H lines are weak and usually disappear after the light curve peak, indicative of a small H mass. Type Ib SNe are SESNe that are H-deficient but exhibit He lines in their spectra, while SNSNe that exhibit neither H nor He lines are categorized as Type Ic SNe. Type Ic-BL SNe are also H- and He-deficient¹, but are categorized by broad spectral lines that are indicative of extremely high velocity ejecta ($\gtrsim 15000 \text{ km s}^{-1}$; [Modjaz et al. 2014](#)). They are the only SN sub-type that is associated with long-duration gamma-ray bursts (*l*GRBs; [Woosley & Bloom 2006](#)).

The progenitor systems of SESNe remain a matter of extensive debate. While they are H-poor, their envelopes could, in principle, be removed either via strong stellar winds or via stripping through interaction with a close binary companion ([Woosley et al. 1995](#)). In the former case, the progenitors of SESNe would predominately be Wolf-Rayet (WR) stars, with initial masses above $25\text{--}30 M_{\odot}$ (e.g. [Begelman & Sarazin 1986](#)). In the latter case, many SESNe could be produced by stars with lower initial masses often associated with H-rich Type II SNe (e.g. $10\text{--}20 M_{\odot}$), but that have lost their envelopes via Roche Lobe Overflow (RLOF) prior to explosion (e.g. [Podsiadlowski et al. 1992](#)).

In recent years, a number of pieces of observational evidence have pointed towards binary stars being a significant contributor to the observed sample of SESNe. First, binary interaction should be common among stars that are expected to be CC SNe progenitors (e.g. [Sana et al. 2012](#)) and SESNe constitute about one-third of all core-collapse SNe in volume-limited samples ([Li et al. 2011](#); [Shivvers et al. 2017](#)). This is higher than the predicted fraction if SESNe solely originate from high-mass WR stars ([Smith et al. 2011](#)). Second, unlike H-rich Type II SNe for which dozens of Red Supergiants (RSGs) have been identified in pre-SN images ([Smartt et al. 2009](#)), direct progenitor detections of SESNe are scarce ([Yoon et al. 2012](#); [Eldridge et al. 2013](#)), indicating the progenitors are relatively faint. While a number of Type IIb progenitors have been identified, they are Yellow Supergiants (YSGs). YSGs are not predicted to explode in standard single star evolution models, and thus may indicate close binary progenitor systems ([Yoon et al. 2017](#); [Sravan et al. 2019](#)). For completely H-stripped SNe, results are even less conclusive. The only reported detections to date are of the progenitors for Type

Ic SN2017ein ([Van Dyk et al. 2018](#); [Xiang et al. 2019](#)) and Type Ib iPTF13bvn ([Cao et al. 2013](#); [Kim et al. 2015](#); [Eldridge & Maund 2016](#)), the former of which has yet to be confirmed. The non-detection of Type Ib/c progenitors in pre-SN images is seemingly in line with the binary scenario where the progenitors are likely to be dim He stars stripped by a companion ([Eldridge et al. 2013](#); [Van Dyk et al. 2016](#)). Lastly, the reported ejecta masses of SESNe are almost exclusively in the range $2\text{--}4 M_{\odot}$ ([Drout et al. 2011](#); [Lyman et al. 2016](#)). These values are lower than those predicted by models of massive single stars stripped by strong stellar winds ($\gtrsim 6 M_{\odot}$ for stars with initial masses of $25\text{--}150 M_{\odot}$; e.g. [Eldridge et al. 2008](#)), but consistent with expectations for lower initial mass stars stripped in binaries².

However, the conclusion that most SESNe are produced by stars from a similar initial mass range as H-rich Type II SNe—simply stripped by a close binary companion—is possibly in tension with other findings. The analyses of H α emission in SN host galaxies reveals that SESNe are more preferably found in star-forming regions compared to H-rich Type II SNe ([Anderson et al. 2012](#)). Further studies of stellar populations in the vicinity of SESNe sites indicate that Type IIb, Ib, and Ic SNe are progressively found in younger stellar populations, suggesting that they arise from more massive progenitors ([Maund 2018](#)). In addition, a key piece of evidence that has been particularly problematic for the binary scenario is the reported ^{56}Ni masses of SESNe, which are systematically larger than those of H-rich Type II SNe ([Anderson 2019](#); [Meza & Anderson 2020](#)). This may suggest that the progenitors of SESNe are initially more massive than those of H-rich Type II SNe, which is more naturally predicted by the evolution of single stars.

Statistical studies of SESNe have reported the average M_{Ni} for SESNe $> 0.1 M_{\odot}$ ([Drout et al. 2011](#); [Lyman et al. 2016](#); [Prentice et al. 2016, 2018](#); [Sharon & Kushnir 2020](#)). Recently, [Anderson \(2019\)](#) compiled the M_{Ni} of 115 H-rich Type II SNe and 141 SESNe reported in the literature. They found the average value of M_{Ni} for SESNe is $0.293 M_{\odot}$ which is a factor of ~ 7 larger than that of H-rich Type II SNe. They argued that this significant discrepancy stems either from differences in the progenitors and explosion mechanisms of Type II versus SESNe or due to systematic errors in the measurement of M_{Ni} values from SN light curves that differ between Type II and SESNe.

Indeed, the accuracy of the M_{Ni} estimates for SESNe has been disputed in recent years ([Dessart et al. 2016](#); [Sukhbold et al. 2016](#); [Khatami & Kasen 2019](#); [Meza & Anderson 2020](#)). Unlike H-rich SNe for which M_{Ni} is estimated by model-

¹ Throughout this paper, Type Ic-BL are not included within Type Ic class.

² Although these results should be interpreted with caution since ejecta masses are often obtained from Arnett-like models, for which some assumptions break down in the case of SESNe as discussed in this paper.

ing the radioactive tail of the light curve, the M_{Ni} of SESNe is commonly obtained from the peak of their bolometric light curves using the models of Arnett (1980, 1982). These are a series of widely-used analytical models for radioactive heating/diffusion based on self-similar assumptions that provide bolometric SN light curves and a consequential rule. This “Arnett’s rule” states that, for SNe powered exclusively by radioactive decay, the radioactive heating rate and the observed bolometric luminosity at the *peak* of the bolometric light curve are equal. Although Arnett’s rule roughly holds for Type Ia SNe, the self-similarity condition breaks down when the SN ejecta has a centralized ^{56}Ni deposition, calling into question its efficacy when applied to SESNe (Khatami & Kasen 2019). Thus, alternate means of measuring M_{Ni} in SESNe may be required.

Most directly, M_{Ni} for SESNe can be measured by modelling the late-time light curve tail, when the ejecta is optically thin and the luminosity is determined by the instantaneous heating rate. However, these epochs have only been observed for a fraction of known SESN. Katz et al. (2013) proposed a “Luminosity Integral” technique for measuring M_{Ni} from radioactively powered SNe, which was recently employed by Sharon & Kushnir (2020) on a dozen SESNe. Although this method does not suffer from many of the simplifying assumptions of Arnett’s models, it relies on the temporally well-sampled observations of SN from the explosion epoch to the tail, and will require the addition of an extra parameter if any other power source significantly contributes to the observed luminosity over this timescale.

Alternatively, Khatami & Kasen (2019, hereafter, KK19) recently proposed a new analytical model that relates the peak bolometric luminosity and its epoch to the radioactive heating function in order to address the limitations of Arnett’s models. However, this model fundamentally depends on the choice of a dimensionless parameter β that is sensitive to several physical effects including the spatial distribution of ^{56}Ni , the envelope composition, potential explosion asymmetries and extra power sources. Meza & Anderson (2020) recently applied the model of KK19 to a sample of SESN, adopting a set of β values that were derived from the simulated SESNe light curves of Dessart et al. (2016). However, to ascertain if those β values are realistic, *they must be directly constrained from observed SESN light curves with independent M_{Ni} estimates*. These observationally calibrated β values would then offer an independent probe of the progenitors and explosion mechanisms of SESN. In addition, if there exists a robust β for each SESN sub-type, then KK19’s model can be used, as an alternative to Arnett’s rule, to give accurate M_{Ni} estimates for a large sample of SESNe.

In this paper, we present a systematic analysis of nickel mass distribution for 27 well-observed SESNe derived by

modeling their radioactive light curve tails, accounting for partial trapping of γ -rays. The resulting M_{Ni} values are then compared against their counterparts measured under Arnett’s rule. We also provide a systematic comparison between the nickel masses of SESNe and H-rich Type II SNe, both obtained from the radioactive light curve tail, hence minimizing the biases that originated from the modeling methods in previous studies. In addition, we employ the model of KK19 on the light curves of observed SESNe to 1) calibrate the β parameter using the peak light curve properties and our independent tail M_{Ni} measurements, and 2) constrain the progenitor and explosion properties of SESNe using our calibrated β in comparison to that obtained from numerical simulations.

This paper is organized as follows. In §2, we describe analytical models that aim to constrain the amount of synthesized ^{56}Ni from light curve observables. §3 presents our criteria for selecting a sample of well-observed SESNe and a systematic procedure for obtaining their distances, extinction values, bolometric light curves, and explosion epochs. We provide the ^{56}Ni masses and calibrated β values for each SN in our sample in §4. We discuss the implications of our results for understanding their progenitor systems and heating sources in §5, and conclude in §6.

2. ANALYTICAL MODELS OF M_{Ni}

To constrain the M_{Ni} of SESNe, we employ three analytical models: an optically-thin radioactive decay model for the light curve tail, Arnett’s rule for the light curve peak, and KK19’s model for the light curve peak. Here, we briefly review their formulation and observational dependencies, as this will influence our SN sample selection in §3.

2.1. Radioactive Decay Modelling of the Light Curve Tail

The “light curve tail” refers to the late-time evolution of the SN light curve once it enters a phase of linear decline in magnitude vs. time. For SESNe, the light curve tail typically begins at an earlier epoch ($t \gtrsim 60$ days post-explosion) compared to H-rich Type II SNe, for which the tail is observable only after the H-recombination plateau phase ends ($t \gtrsim 90$ days post-explosion). It is widely thought that the tail of core-collapse SNe is powered by the $^{56}\text{Co} \rightarrow ^{56}\text{Fe}$ radioactive decay chain (Colgate & McKee 1969). At this stage, the ejecta become transparent to the stored radiative energy; therefore, the observed luminosity traces the instantaneous heating rate. The γ -rays produced by the radioactive decay heat the ejecta, making the tail of the light curve an appropriate probe for measuring the amount of ^{56}Ni produced. The observed luminosity of the tail can be then modeled as:

$$L \simeq L_{\gamma} (1 - e^{-(t/T_0)^2}) + L_{\text{pos}}, \quad (1)$$

(Wygoda et al. 2019), where t is time since the explosion, L_γ is the luminosity produced by the radioactive decay of Co^{56} and Ni^{56} , and L_{pos} is the total energy release rate of positron kinetic energy. The term in parenthesis is a deposition factor, which represents the incomplete trapping of γ -rays with T_0 denoting the partial trapping timescale of the tail. The deposition factor is proportional to $1 - e^{-t/T_0}$ for an explosion in homologous expansion (Sutherland & Wheeler 1984; Clocchiatti & Wheeler 1997). The luminosity terms in Equation 1 can be expressed as:

$$L_\gamma = M_{\text{Ni}} \left((\epsilon_{\text{Ni}} - \epsilon_{\text{Co}}) e^{-t/t_{\text{Ni}}} + \epsilon_{\text{Co}} e^{-t/t_{\text{Co}}} \right) \quad (2)$$

$$L_{\text{pos}} = 0.034 M_{\text{Ni}} \epsilon_{\text{Co}} \left(e^{-t/t_{\text{Ni}}} - e^{-t/t_{\text{Co}}} \right), \quad (3)$$

where $\epsilon_{\text{Ni}} = 3.9 \times 10^{10} \text{ erg g}^{-1} \text{ s}^{-1}$ and $\epsilon_{\text{Co}} = 6.8 \times 10^9 \text{ erg g}^{-1} \text{ s}^{-1}$ are the specific heating rates of Ni and Co decay, respectively, and $t_{\text{Ni}} = 8.8$ days and $t_{\text{Co}} = 111.3$ days are their corresponding decay timescales. In this formulation, the escape of positrons, which happens on the timescale of several hundred days, is ignored. While the complete trapping of γ -rays is commonly assumed for H-rich Type II SNe due to their large ejecta masses and correspondingly long T_0 , it is important to determine the T_0 from the slope of light curve tail for SESNe since their ejecta masses are smaller and T_0 is usually comparable to the onset time of the radioactive tail. If the bolometric luminosity L can be ascertained observationally, the only unknowns in Equations 1 and 2 are M_{Ni} and T_0 which can be determined by fitting the slope and overall normalization of the radioactive tail of the light curve.

2.2. Arnett's Rule

While robust, the “light curve tail” method is not always accessible because the late-time radioactive tails are often faint, and thus more difficult to observe. As a result, the M_{Ni} of SESNe are typically obtained with Arnett's rule, which states that the instantaneous heating rate from the radioactive decay of ^{56}Ni and ^{56}Co is equal to the bolometric luminosity of the SN at the light curve peak. This can be rewritten as:

$$L_p = M_{\text{Ni}} \left((\epsilon_{\text{Ni}} - \epsilon_{\text{Co}}) e^{-t_p/t_{\text{Ni}}} + \epsilon_{\text{Co}} e^{-t_p/t_{\text{Co}}} \right), \quad (4)$$

where t_p and L_p are the peak time and peak bolometric luminosity, respectively. Arnett-like models make several assumptions to solve the thermodynamic differential equation, including homologous expansion of the ejecta, radiation-dominated pressure, spherical symmetry, and a self-similar energy density profile and also adopt a radiation diffusion approximation (Arnett 1980, 1982).

2.3. KK19's model

KK19 showed that the assumption of self-similarity for the energy density profile will limit the accuracy of the Arnett-like models, especially for centrally-located heating sources, due to the time-dependent evolution of the diffusion wave through the ejecta. Instead, they propose a new relationship between the peak time, t_p , and peak luminosity, L_p , without assuming self-similarity:

$$L_p = \frac{2}{\beta^2 t_p^2} \int_0^{\beta t_p} t' L_{\text{heat}}(t') dt' \quad (5)$$

where $L_{\text{heat}}(t)$ denotes a generic heating function and β is a dimensionless parameter of an order of unity. When $L_{\text{heat}}(t)$ is powered by $^{56}\text{Ni} \rightarrow ^{56}\text{Co} \rightarrow ^{56}\text{Fe}$ radioactive decay, Equation 5 becomes:

$$L_p = \frac{2\epsilon_{\text{Ni}} M_{\text{Ni}} t_{\text{Ni}}^2}{\beta^2 t_p^2} \left[\left(1 - \frac{\epsilon_{\text{Co}}}{\epsilon_{\text{Ni}}} \right) \left(1 - (1 + \beta t_p/t_{\text{Ni}}) e^{-\beta t_p/t_{\text{Ni}}} \right) \right. \\ \left. + \frac{\epsilon_{\text{Co}} t_{\text{Co}}^2}{\epsilon_{\text{Ni}} t_{\text{Ni}}^2} \left(1 - (1 + \beta t_p/t_{\text{Co}}) e^{-\beta t_p/t_{\text{Co}}} \right) \right]. \quad (6)$$

For this specific form of $L_{\text{heat}}(t)$, the following relationships hold: The M_{Ni} required to reproduce a fixed $\{t_p, L_p\}$ pair will be directly proportional to the β value adopted. In contrast, if M_{Ni} is known, then the value of L_p or t_p required to reproduce a given $\{t_p, M_{\text{Ni}}\}$ or $\{L_p, M_{\text{Ni}}\}$ pair, respectively, will be *inversely* proportional to the value of β adopted (if the light curve is powered entirely by radioactive decay).

The parameter β incorporates the fact that L_p does not necessarily trace the radioactive heating rate as the stored internal energy of ejecta may lag or lead the observed luminosity, $L(t)$, at the time of peak. The choice of β critically depends on several physical effects such as the spatial distribution of ^{56}Ni , the envelope composition, asymmetries in the heating source or ejecta, and all power sources contributing to the observed luminosity along with their exact heating functions. Using Equation 6, β can be derived from the light curve of SESNe with known L_p and t_p , if there is an independent constraint on M_{Ni} . We can then observationally calibrate the appropriate values of β using a sample of SESNe of various sub-types. With a sample of calibrated β values, one can potentially apply KK19's model to a wide range of SESNe with only photospheric data coverage to constrain their M_{Ni} . In addition, comparing the β values obtained from observed SESN light curves to those inferred from numerical light curve models calculated with different input physics can inform us about the explosion details of SESNe.

3. SN SAMPLE AND METHODS

3.1. Sample Selection

Our SESN sample should consist of those SESNe for which a measurement of the M_{Ni} can be made from both

the light curve tail and the light curve peak. This will allow us to conduct an empirical comparison between the M_{Ni} of SESNe obtained from the Arnett model and the radioactive tail and also provides the means to produce a data-driven calibration of the KK19 β values for SESN. Therefore, we compiled the photometry of well-observed SESNe in the literature and select SESNe that meet the following criteria:

1. well-sampled coverage of the early rise (i.e., multiple observations before 5 days pre-maximum in at least one band) or the observation of an accompanying GRB/X-ray flash, since a constraint on the epoch of explosion is needed to derive M_{Ni} from Equations 1 and 2,
2. multiple photometric measurements on the tail of the light curve, i.e., epochs $\gtrsim 60$ days, to be able to obtain M_{Ni} from the radioactive tail,
3. reasonable coverage around the light curve peak, which is required for both computing M_{Ni} using the Arnett model (Equation 4) and calibrating the β parameter using KK19's model (Equation 6),
4. light curves in at least two bands over the light curve tail and peak, so that the bolometric luminosity and host galaxy reddening can be computed. (See § 3.5 for the method.)

We identified 27 SNe from the literature that satisfy the above criteria and downloaded their photometric data from The Open Supernova Catalog (Guillochon et al. 2017). Our sample consists of 8 IIb, 8 Ib, 4 Ic, and 7 Ic-BL SNe. These SNe are listed in Table 1 along with their basic properties, including SN type, the host galaxy name, distance estimate, extinction, and the epoch of explosion.

3.2. Distances

The distances we adopt throughout our analyses are listed in Table 1. We adopt up-to-date host galaxy distances reported in NASA/IPAC Extragalactic Database (NED)³. We prioritize distances obtained by Cepheids and Tip of Red Giant Branch methods when available and otherwise use cosmology-dependent values. For redshift-dependent distances, we adopt the standard Λ CDM cosmology with a Hubble constant $H_0 = 73.24 \text{ km s}^{-1} \text{ Mpc}^{-1}$, matter density parameter $\Omega_M = 0.27$, vacuum density parameter $\Omega_\Lambda = 0.73$ (Riess et al. 2016) and correct for Virgo, Great Attractor, and Shapley Supercluster Infall. For one object (SN2006el, which exploded in the galaxy UGC 12188), no host galaxy redshift is listed in NED. We therefore adopt the distance

given in Drout et al. (2011), which is based on a host galaxy redshift reported in ATel 854 (Antilogus et al. 2006).

3.3. Galactic and Host Galaxy Extinction

We adopt the value for galactic extinction along the line of sight to each SN reported in NASA/IPAC Infrared Science Archive⁴ based on the extinction model of Schlafly & Finkbeiner (2011) and assuming an $A_V/E(B-V) = 3.1$ extinction law. The resulting values are listed in Table 1.

To estimate values for host galaxy extinction, we use the intrinsic SN color-curve templates of Stritzinger et al. (2018) and attribute the difference between the observed and the intrinsic color to the host galaxy reddening. Specifically, the host extinction can be written in terms of the observed minus intrinsic color as: $E(X - Y)_{\text{host}} = (X - Y)_{\text{obs}} - (X - Y)_{\text{int}}$, where X and Y are the measured magnitudes corrected for the Galactic extinction in two different filters. When computing the extinction, we take the average of the color difference between the observed data and the templates of Stritzinger et al. (2018) from 5 days to 10 days post-maximum. When determining this average, time of maximum is defined based on the observed filter that we adopt as the “ X ”-band in the above expression.

Whenever available, we use $X - Y = V - R/r/i$ color indices. Since there is no template provided for $V - R$ intrinsic color in Stritzinger et al. (2018), we convert observed Johnson R -band photometry to Sloan r -band using the color transformation relation of Jordi et al. (2006) when required. $E(X - Y)$ is then converted to the standard reddening $E(B - V)$ using the bandpass coefficients of Schlafly & Finkbeiner (2011). For those SNe for which photometric data is not available in any of the $R/r/i$ filters, we adopt $B - V$ color index instead. Furthermore, we find that our obtained reddening is not robust to the choice of filters X and Y for several Type IIb SNe (i.e., SN1993J, SN2011dh, and SN2013df). For these SNe, we take the average of $E(B - V)$ values derived using different color indices such as $V - r$, $V - i$, and $B - V$. The final host galaxy extinctions used in our analyses are listed in Table 1.

3.4. Epoch of Explosion

The estimated epochs of explosion for each SN are presented in Table 1. For several of Type IIb SNe with double-peaked light curves, the epoch of explosion is adopted from the reported values obtained from by modeling the shock cooling emission. For SN1998bw, which is a Type Ic-BL SN associated with GRB 980425, we take the GRB epoch as the explosion epoch. Similarly, for SN2008D, the epoch of the observed X-ray flash XRO080109 is taken as the explosion epoch. Since the shock velocities of these SNe are high, we

³ <https://ned.ipac.caltech.edu/>

⁴ <https://irsa.ipac.caltech.edu/applications/DUST/>

Table 1. SESN sample with their basic parameters

SN name	Host	Type	d (Mpc)	Galactic $E(B-V)$ (mag)	Host $E(B-V)$ (mag)	t0 (MJD)
SN1993J	M81	IIb	3.6 (0.2) ^a	0.0690 (0.0001)	0.11 (0.00)	49074.0 (0.0) ^c
SN1994I	M51	Ic	8.6 (0.1) ^a	0.0308 (0.0015)	0.40 (0.04)	49443.5 (0.3)
SN1996cb	NGC 3510	IIb	9.8 (0.7)	0.0261 (0.0005)	0.00 (0.01)	50429.5 (2.0)
SN1998bw	ESO 184-G82	Ic-BL	38.1 (2.6)	0.0494 (0.0011)	0.00 (0.02)	50928.9 (0.0) ^d
SN2002ap	M74	Ic-BL	9.8 (0.5) ^a	0.0616 (0.0018)	0.01 (0.02)	52300.0 (2.5)
SN2003jd	MCG -01-59-21	Ic-BL	77.9 (5.4)	0.0378 (0.0005)	0.00 (0.10)	52929.0 (2.0)
SN2004aw	NGC 3997	Ic	73.6 (5.0)	0.0184 (0.0009)	0.37 (0.08)	53076.5 (6.0)
SN2004gq	NGC 1832	Ib	26.3 (1.8)	0.0629 (0.0004)	0.12 (0.02)	53346.1 (4.0)
SN2005hg	UGC 1394	Ib	87.7 (6.0)	0.0894 (0.0021)	0.52 (0.08)	53665.6 (2.0)
SN2006T	NGC 3054	IIb	34.6 (2.4)	0.0643 (0.0007)	0.26 (0.03)	53764.5 (1.5)
SN2006el	UGC 12188	IIb	70.0 (7.0) ^b	0.0975 (0.0012)	0.07 (0.04)	53962.3 (0.7)
SN2006ep	NGC 214	Ib	61.7 (4.3)	0.0306 (0.0005)	0.33 (0.05)	53970.5 (7.0)
SN2007gr	NGC 1058	Ic	9.0 (0.6)	0.0532 (0.0005)	0.15 (0.11)	54329.7 (2.5)
SN2007ru	UGC 1238	Ic-BL	60.9 (4.2)	0.2217 (0.0046)	0.00 (0.02)	54429.5 (3.0)
SN2007uy	NGC 2770	Ib	31.4 (2.2)	0.0192 (0.0003)	0.53 (0.02)	54464.0 (3.5)
SN2008D	NGC 2770	Ib	31.4 (2.2)	0.0193 (0.0002)	0.47 (0.04)	54474.6 (0.0) ^e
SN2008ax	NGC 4490	IIb	9.2 (0.6)	0.0188 (0.0002)	0.25 (0.04)	54528.3 (1.0)
SN2009bb	NGC 3278	Ic-BL	40.1 (2.8)	0.0847 (0.0010)	0.40 (0.08)	54912.9 (1.1)
SN2009jf	NGC 7479	Ib	33.8 (2.4)	0.0970 (0.0013)	0.07 (0.06)	55099.5 (4.2)
SN2011bm	IC 3918	Ic	99.2 (6.8)	0.0285 (0.0005)	0.00 (0.15)	55645.5 (0.5)
SN2011dh	M51	IIb	8.6 (0.1) ^a	0.0309 (0.0017)	0.15 (0.03)	55712.0 (0.0) ^c
iPTF13bvn	NGC 5806	Ib	23.9 (1.7)	0.0436 (0.0006)	0.15 (0.04)	56458.3 (0.8)
SN2013df	NGC 4414	IIb	17.9 (1.0) ^a	0.0168 (0.0002)	0.20 (0.04)	56447.3 (0.9) ^c
SN2013ge	NGC 3287	Ib	23.7 (1.6)	0.0198 (0.0002)	0.10 (0.10)	56602.3 (4.7)
SN2014ad	PGC 37625	Ic-BL	26.7 (1.9)	0.0380 (0.0012)	0.10 (0.07)	56724.5 (3.0)
SN2016coi	UGC 11868	Ic-BL	18.1 (1.3)	0.0737 (0.0021)	0.27 (0.08)	57533.2 (2.1)
SN2016gkg	NGC 613	IIb	19.7 (1.4)	0.0166 (0.0002)	0.20 (0.17)	57655.2 (0.0) ^c

^aRedshift-independent distances. SN1993J and 2013df (Gerke et al. 2011); SN1994I and 2011df (McQuinn et al. 2016); SN2002ap (McQuinn et al. 2017)

^bDistance from the value reported in Drout et al. (2011)

^cEpoch of explosion from the shock cooling emission

^dEpoch of explosion from the GRB emission

^eEpoch of explosion from the X-ray emission

NOTE—References: SN1993J (Richmond et al. 1994, 1996a); SN1994I (Richmond et al. 1996b); SN1996cb (Qiu et al. 1999); SN1998bw (Galama et al. 1998; McKenzie & Schaefer 1999); SN2002ap (Pandey et al. 2003; Yoshii et al. 2003); SN2003jd (Valenti et al. 2008); SN2004aw (Taubenberger et al. 2006); SN2004gq (Bianco et al. 2014; Stritzinger et al. 2018); SN2005hg (Drout et al. 2011); SN2006T (Stritzinger et al. 2018); SN2006el (Drout et al. 2011; Bianco et al. 2014); SN2006ep (Bianco et al. 2014; Stritzinger et al. 2018); SN2007gr (Hunter 2007); SN2007ru (Sahu et al. 2009); SN2007uy (Bianco et al. 2014); SN2008D (Bianco et al. 2014); SN2008ax (Pastorello et al. 2008); SN2009bb (Pignata et al. 2011); SN2009jf (Sahu et al. 2011); SN2011bm (Valenti et al. 2012); SN2011dh (Tsvetkov et al. 2012); iPTF13bvn (Folatelli et al. 2016; Fremling et al. 2016); SN2013df (Morales-Garoffolo et al. 2014; Shivvers et al. 2019); SN2013ge (Drout et al. 2011); SN2014ad (Sahu et al. 2018); SN2016coi (Prentice et al. 2018); SN2016gkg (Bersten et al. 2018);

can assume that the GRB or X-ray flash occurs shortly after the explosion time; therefore, GRB 980425 and XRO080109 provide accurate estimates of the explosion epochs. For the rest of SNe in our sample, we estimate the explosion time by fitting a power-law with the form:

$$f = \begin{cases} f_0(t - t_0)^n & t > t_0 \\ 0 & t \leq t_0 \end{cases}, \quad (7)$$

to the observed fluxes, f , in the band with the best early light curve coverage. We carry out least-square regression to fit for the power index n , scaling coefficient f_0 , and

epoch of explosion t_0 . For the fitting, we only consider epochs that are pre-maximum-light and within 5 days of the first reported detection as well as any publicly available non-detection upper limits. The uncertainties on the explosion epoch quoted in Table 1 come directly from the fitting process. The consequences of a possible “dark phase” (Piro & Nakar 2013) between the explosion epoch and the epoch of first light will be discussed in § 5.1.1.

3.5. Bolometric Light Curves

The relative paucity of SESN with extensive coverage in UVOIR bands from early to late times is a challenge for

Table 2. The fit parameters for the SESN sample

SN name	Type	BC bands	$\log L_p$ (erg s $^{-1}$)	t_p (days)	Tail M_{Ni} (M_{\odot})	T_0 (days)	Arnett M_{Ni} (M_{\odot})	Calibrated β	KK19 M_{Ni} (M_{\odot}) ¹	f
SN1993J	IIb	$V - I$	42.41 (41.56)	22.0 (0.0)	0.081 (0.005)	110.9 (9.9)	0.15 (0.02)	0.80 (0.16)	0.80 (0.16)	0.23
SN1994I	Ic	$V - I$	42.62 (41.56)	8.2 (0.3)	0.048 (0.015)	57.0 (10.3)	0.11 (0.01)	0.00 (0.00)	0.080 (0.007)	0.48
SN1996cb	IIb	$V - R$	41.87 (41.12)	21.7 (2.0)	0.030 (0.003)	96.8 (14.6)	0.04 (0.01)	1.17 (0.27)	0.023 (0.004)	-0.01
SN1998bw	Ic-BL	$V - I$	43.16 (42.38)	16.6 (0.0)	0.300 (0.013)	108.9 (14.5)	0.67 (0.11)	0.50 (0.19)	0.312 (0.052)	0.38
SN2002ap	Ic-BL	$V - I$	42.47 (41.60)	13.1 (2.5)	0.062 (0.003)	113.4 (12.3)	0.11 (0.02)	0.64 (0.20)	0.058 (0.008)	0.27
SN2003jd	Ic-BL	$V - R$	42.85 (42.11)	15.0 (2.1)	0.117 (0.014)	101.4 (16.1)	0.29 (0.06)	0.29 (0.21)	0.145 (0.026)	0.47
SN2004aw	Ic	$V - I$	42.71 (41.93)	15.6 (6.0)	0.151 (0.030)	150.1 (92.0)	0.22 (0.07)	1.03 (0.26)	0.133 (0.022)	0.08
SN2004gq	Ib	$B - V$	42.36 (41.67)	12.3 (4.0)	0.044 (0.008)	144.6 (74.2)	0.08 (0.03)	0.59 (0.32)	0.051 (0.011)	0.29
SN2005hg	Ib	$V - R$	43.09 (42.34)	18.8 (2.0)	0.353 (0.039)	143.2 (19.2)	0.63 (0.13)	0.83 (0.23)	0.348 (0.063)	0.21
SN2006T	IIb	$B - V$	42.63 (42.00)	15.5 (1.5)	0.082 (0.012)	143.6 (29.5)	0.18 (0.05)	0.49 (0.30)	0.105 (0.025)	0.39
SN2006el	IIb	$V - r^2$	42.27 (41.63)	21.4 (0.7)	0.052 (0.005)	126.4 (21.2)	0.11 (0.02)	0.70 (0.25)	0.057 (0.013)	0.31
SN2006ep	Ib	$B - V$	42.55 (41.83)	15.0 (7.0)	0.058 (0.015)	112.2 (31.1)	0.16 (0.07)	0.29 (0.22)	0.088 (0.017)	0.47
SN2007gr	Ic	$V - I$	42.38 (41.60)	9.8 (2.5)	0.047 (0.004)	126.9 (15.7)	0.07 (0.02)	0.77 (0.33)	0.049 (0.008)	0.18
SN2007ru	Ic-BL	$V - I$	42.90 (42.13)	11.1 (3.0)	0.103 (0.009)	107.7 (14.9)	0.27 (0.07)	0.09 (0.13)	0.147 (0.025)	0.50
SN2007uy	Ib	$B - V$	42.80 (42.16)	16.1 (3.5)	0.143 (0.024)	119.9 (25.4)	0.29 (0.09)	0.64 (0.29)	0.166 (0.037)	0.31
SN2008D	Ib	$V - r^2$	42.08 (41.32)	19.9 (0.2)	0.036 (0.003)	104.6 (14.1)	0.07 (0.01)	0.82 (0.21)	0.036 (0.006)	0.22
SN2008ax	IIb	$V - R$	42.31 (41.58)	21.8 (1.2)	0.060 (0.009)	99.2 (17.2)	0.12 (0.02)	0.73 (0.21)	0.063 (0.012)	0.29
SN2009bb	Ic-BL	$V - I$	42.78 (42.01)	11.0 (1.1)	0.158 (0.055)	47.8 (14.5)	0.19 (0.04)	1.23 (0.35)	0.109 (0.019)	-0.04
SN2009jf	Ib	$V - I$	42.68 (41.91)	22.3 (4.2)	0.164 (0.022)	158.3 (22.7)	0.29 (0.07)	0.87 (0.20)	0.155 (0.026)	0.19
SN2011bm	Ic	$V - I$	42.86 (42.09)	34.6 (0.7)	0.574 (0.038)	119.3 (90.3)	0.63 (0.11)	1.71 (0.41)	0.336 (0.057)	-0.33
SN2011dh	IIb	$V - R$	42.49 (41.48)	20.1 (0.0)	0.093 (0.002)	102.0 (8.6)	0.17 (0.02)	0.81 (0.12)	0.090 (0.009)	0.22
iPTF13bvn	Ib	$V - I$	42.31 (41.54)	16.7 (0.8)	0.040 (0.006)	134.9 (15.6)	0.10 (0.02)	0.43 (0.19)	0.055 (0.009)	0.42
SN2013df	IIb	$V - I$	42.37 (41.53)	22.6 (1.6)	0.063 (0.004)	128.2 (12.6)	0.14 (0.02)	0.61 (0.14)	0.074 (0.011)	0.37
SN2013ge	Ib	$B - V$	42.39 (41.78)	16.8 (4.7)	0.063 (0.012)	122.8 (31.3)	0.11 (0.04)	0.79 (0.33)	0.065 (0.016)	0.24
SN2014ad	Ic-BL	$V - I$	42.84 (42.07)	16.4 (3.0)	0.147 (0.023)	96.7 (15.6)	0.32 (0.08)	0.54 (0.20)	0.148 (0.025)	0.36
SN2016coi	Ic-BL	$V - I$	42.84 (42.06)	17.6 (2.1)	0.170 (0.016)	135.7 (18.3)	0.34 (0.07)	0.67 (0.20)	0.153 (0.026)	0.30
SN2016gkg	IIb	$V - I$	42.29 (41.51)	16.5 (4.0)	0.055 (0.004)	124.8 (15.5)	0.09 (0.02)	0.91 (0.24)	0.050 (0.008)	0.15

¹ M_{Ni} values obtained from KK19's model assuming the median values of calibrated β reported in Table 4 (see § 4.4).² Since the BCs provided by Lyman et al. (2014) are given in Johnson bands, magnitudes in Sloan r are first converted to Johnson R using the transformations of Jordi et al. (2006).

computing bolometric light curves that are needed to obtain M_{Ni} . Here, we focus on obtaining the bolometric luminosities for epochs around the light curve peak and the late-time tail. In order to leverage the multi-band photometric data available for our SESNe sample, we adopt the bolometric correction (BC) coefficients of Lyman et al. (2014, 2016). These color-dependent coefficients were measured by fitting the SEDs of a sample of SESNe that have coverage in ultra-violet, optical, and infrared wavelengths, and can be utilized as long as light curves for a SN of interest are available in a minimum of two bands.

We first compute the absolute magnitude light curves for all SN in our sample in the pair of bands indicated in Table 2 (column “BC bands”). We correct for the distances and total line-of-sight extinction described above. Next, we fit the multi-band absolute magnitude light curves around the peak and over the radioactive tail with a spline-smoothing function and linear function, respectively. We perform a Monte Carlo (MC) analysis to propagate the un-

certainties in the measured magnitudes and distance estimate. The fitted absolute magnitude light curves, which together also provide intrinsic color as function of time, are then used to calculate a bolometric magnitude light curve by applying the color-dependent BC polynomials of Lyman et al. (2014, 2016). Specifically, $M_{\text{bol}} = M_X + \text{BC}$, where the BC is computed using the color indices listed in column “BC bands” of Table 2, and X denotes the first indicated band listed in that column. Finally, we convert bolometric magnitudes to luminosities assuming $M_{\text{bol},\odot} = 4.74$ mag and $L_{\text{bol},\odot} = 3.83 \times 10^{33}$ erg s $^{-1}$.

Figure 1 illustrates this process. It presents the absolute magnitude (top panel) and the resulting bolometric (bottom panel) light curves for two SNe in our sample: SN2008ax and SN2007ru. These two objects were specifically chosen to span the range of light curve coverage available during the early rise and late-time tail for SN in our sample. The spline and linear fits to the absolute magnitude light curves are shown in the top panel. The x-axis

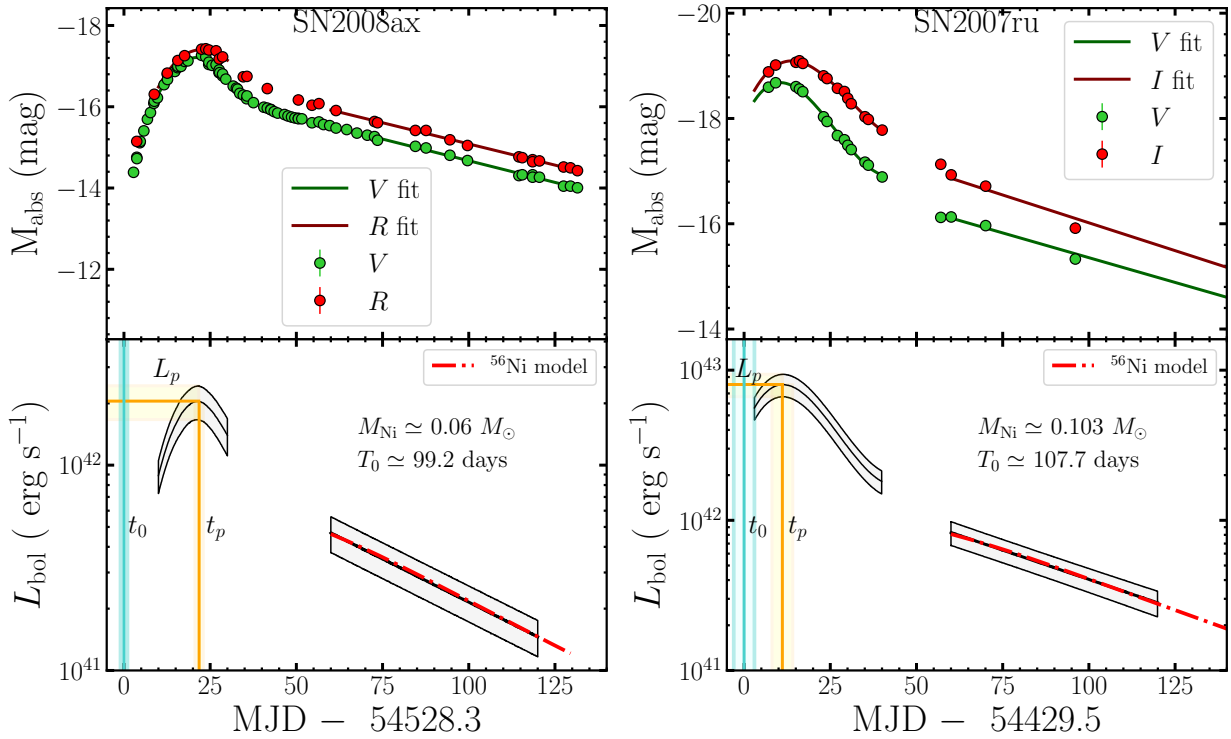


Figure 1. Extinction-corrected absolute magnitude (top panel) and bolometric luminosity (bottom panel) light curves for SN2008ax (left panel) and SN2007ru (right panel). The green and red solid curves represent fits to the absolute magnitudes in V and R/I bands, respectively. The cyan vertical line indicates the epoch of explosion t_0 , while the vertical and horizontal orange lines denote the peak time t_p and peak luminosity L_p of the bolometric light curves, respectively. The 1- σ confidence level in t_0 , t_p , and L_p are shown with cyan and orange strips. The dot-dashed red curve in the lower panels represents the best-fit ^{56}Ni model of Equation 1 to the bolometric radioactive tails (see annotation for fit parameters). Note when error bars are not visible in the top panel they are smaller than the plotted points.

represents time since the inferred epoch of explosion derived in § 3.4. Gray regions indicate the uncertainties in the bolometric luminosity obtained at each epoch. These uncertainties stem from (in decreasing order of importance): error in the distance estimate, BC error, and photometric error. We also mark the epoch of explosion t_0 , the peak luminosity L_p and peak time t_p of the bolometric light curve in the bottom panel, with shaded regions representing the uncertainty on each parameter.

Derived values of L_p and t_p for each SN are listed in Table 2, and plotted in Figure 2. Note that the final error in t_p is a combination of the error in the t_0 and bolometric light curve. Overall, the peak luminosities for our sample span $10^{41.87}\text{--}10^{43.09}$ erg s^{-1} and rise times span 8.2–34.6 days (SN1994I and SN2011bm, respectively). As seen in Figure 2, no correlation is apparent between L_p and t_p for the SESNe in our sample.

Comparing our L_p estimates with previous studies, we find that our derived peak luminosities are a factor ~ 2 larger than those found by Meza & Anderson (2020) who integrate luminosity over the BVRIJH bands, but they are in good agreement with those of Prentice et al. (2016) who find peak luminosities by summing over the UBVRIJHK bands for a fraction of their SN sample. In addition, our

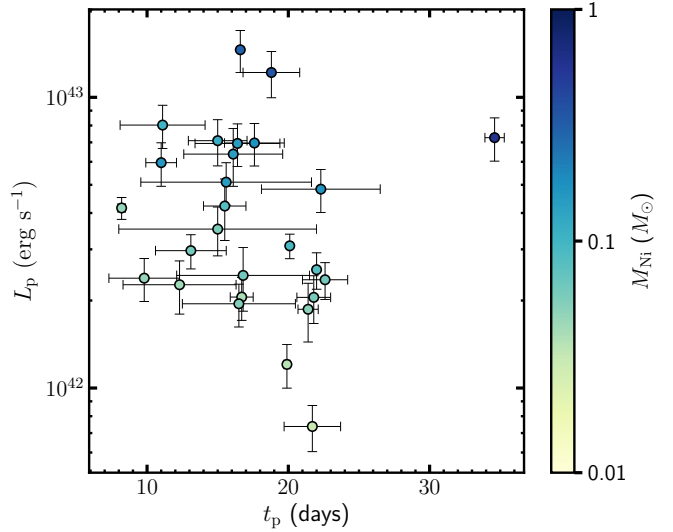


Figure 2. Peak time, t_p , versus peak luminosity, L_p , for our sample of SESNe. Markers are color-coded based on their tail M_{Ni} value.

L_p estimates are consistent within our quoted errors with those of Lyman et al. (2016), who also adopt the BC polynomial fits of Lyman et al. (2014).

4. RESULTS

4.1. Nickel Masses from the Radioactive Tail

To constrain M_{Ni} of our SESNe sample, we model their radioactive light curve tails using the analytic model of Wygoda et al. (2019) discussed in § 2. This model is similar to those of Valenti et al. (2008) and Drout et al. (2013) with one minor modification: the positrons' escape is neglected. Since positrons' escape occurs on a time scale of a few thousand days, it should not affect our results.

By fitting the bolometric luminosity and slope of the radioactive tail for the SESN sample, we can constrain the two unknown parameters in Equation 1: the nickel mass, M_{Ni} , and partial trapping timescale of the tail, T_0 . The fitting is done in an MC fashion: we run 1000 trials drawing from the distribution of possible luminosities and epochs of explosion. This allows us to propagate the uncertainties in these quantities when obtaining M_{Ni} and T_0 . We only consider epochs of ≥ 60 days post-explosion, when the ejecta of SESNe are expected to be optically thin, such that the bolometric luminosity will be set by the instantaneous heating rate. In Figure 1, we display the best-fit radioactive tail models for SN 2008ax and SN 2007ru (dot-dashed red curves; bottom panels). As shown, the model closely matches the evolution of the bolometric radioactive tail. The best-fit parameters, “tail M_{Ni} ” and T_0 , for each SN are listed in Table 2. Our best-fit tail M_{Ni} values range from $\sim 0.030 M_{\odot}$ to $\sim 0.574 M_{\odot}$ with a median value of $0.08 M_{\odot}$. T_0 is in the range ~ 47.8 – 158.3 days with a median value of 116.6 days. The points in Figure 2 are color-coded based on these derived tail M_{Ni} values. Objects with larger M_{Ni} values also exhibit brighter peak luminosities, as expected for SNe powered predominately by radioactive decay.

We report the basic statistics of our results (mean, median, and standard deviation) for both the full sample and separated by SESN sub-type in Table 3. However, we note that our sample size is relatively small when SNe are categorized by sub-types; especially normal Type Ic SNe, for which only 4 events met all of our sample criteria outlined in § 3.1 and whose distribution may be skewed by the extreme event SN 2011bm. Therefore, we conduct Analysis of Variance (ANOVA) test to check whether the reported differences between the mean M_{Ni} of SN sub-types are statistically significant. The result of ANOVA test indicates that the pairwise comparison of M_{Ni} between SN sub-types is not generally statistically significant. One exception for Type Ic-BL SNe for which the reported mean M_{Ni} was found to be higher than that of the combined sample of all other SESN sub-types with p-value < 0.05 . This is consistent with previous studies which have typically found systematically higher M_{Ni} for Type Ic-BL events (e.g. Drout et al. 2011; Lyman et al. 2016; Prentice et al. 2016).

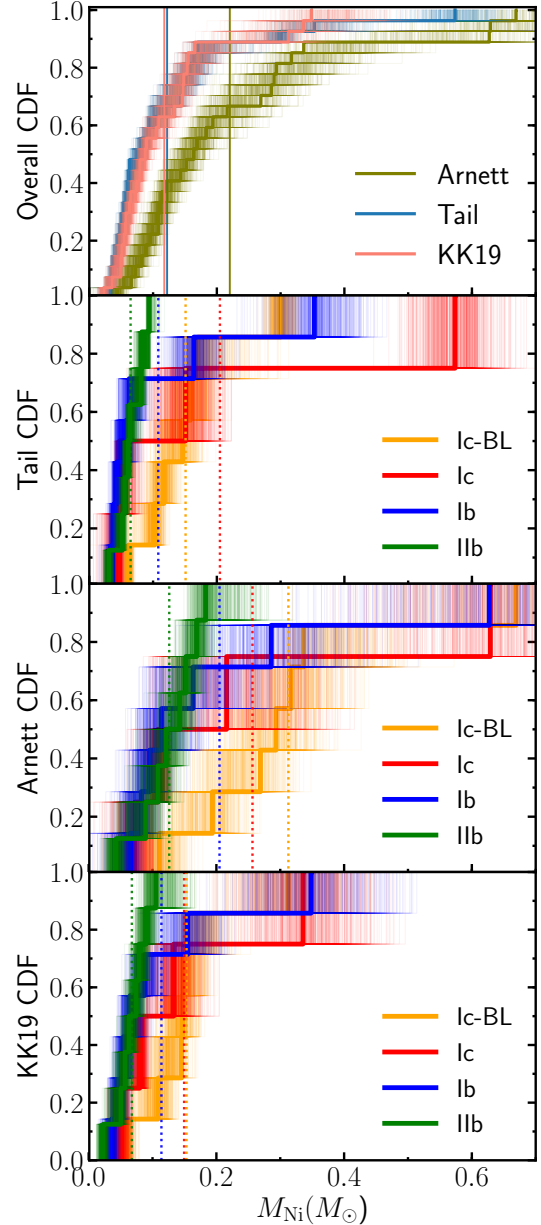


Figure 3. Cumulative Distribution Functions of M_{Ni} . *Top:* The M_{Ni} CDFs obtained using the radioactive tail modeling (blue curve), Arnett's rule (olive curve), and KK19 model (pink curve). *Middle top:* The tail M_{Ni} CDFs categorized into the SN types: Type Ic-BL (yellow curve), Ic (red curve), Ib (blue curve), and IIb (green curve). *Middle bottom & bottom:* same as the middle top panel but for Arnett and KK19 CDFs, respectively. KK19 M_{Ni} values are obtained using the median values of calibrated β (see § 4.4). The vertical lines show the mean of each distribution. The hatched regions represent the uncertainties in CDFs.

Figure 3 displays Cumulative Distribution Functions (CDFs) of the derived M_{Ni} for our sample of SESNe. In the top panel of Figure 3, the M_{Ni} CDFs are provided for the entire SESN sample obtained using multiple methods: radioactive tail modeling (blue), Arnett's rule (green), and

Table 3. Table of ^{56}Ni Mass Statistics

SN Type	Tail M_{Ni} (M_{\odot})			Arnett M_{Ni} (M_{\odot})			KK19 M_{Ni} (M_{\odot})		
	Mean	Median	Std	Mean	Median	Std	Mean	Median	Std
IIb	0.06	0.06	0.02	0.13	0.13	0.04	0.07	0.07	0.02
Ib	0.11	0.06	0.11	0.20	0.11	0.19	0.12	0.08	0.1
Ic	0.20	0.10	0.22	0.26	0.16	0.22	0.15	0.11	0.11
Ic-BL	0.15	0.15	0.07	0.31	0.29	0.16	0.15	0.15	0.07
All	0.12	0.08	0.12	0.22	0.16	0.17	0.12	0.09	0.09

KK19 model (pink). (See 4.2 and 4.5 for Arnett and KK19 methods, respectively.) In order to account for the errors in individual M_{Ni} measurements when plotting the CDFs, we run 1000 MC trials in which we sample each M_{Ni} value based on the distribution defined by its uncertainty and construct a new CDF. These sampled CDFs are over-plotted in Figure 3, forming hatched regions that represent the uncertainties associated with the obtained CDFs.

In the second panel of Figure 3 we present the CDFs of the tail M_{Ni} values for each SESN sub-types separately. We conduct Kolmogorov-Smirnov (K-S) tests on the CDFs of tail M_{Ni} estimates for each sub-type. A K-S test on the CDF of Type Ic-BL and Ib/c SNe rejects the null hypothesis that these SN types are drawn from the same groups of explosions with a p-value = 0.02. In contrast, we find that Type Ic and Ib SNe are likely to be drawn from the same distributions with p-value = 0.24. Similarly, a K-S test on Type IIb and Ib/c SNe supports the null hypothesis that these samples originate from the same distribution with p-value = 0.10. The p-value further increases to 0.45 when we compare the CDF of Type IIb and Ib SNe.

Radioactive tail nickel masses have previously been estimated for a number of SN in our sample, and results are consistent. In particular, the tail M_{Ni} values reported in the recent work of Meza & Anderson (2020) are lower limits as they do not take the partial trapping of γ -rays into account. Our tail M_{Ni} estimates provided in Table 2 are consistent with these lower limits for SNe that are shared between both samples. Similarly, our M_{Ni} and T_0 estimates are consistent with (within the margin of error) those obtained from the Katz Integral method (Sharon & Kushnir 2020) for 8 SESNe in common between the samples.

4.2. Comparison to Arnett Model

For comparison, we also measure M_{Ni} using Arnett's rule, described in § 2, which has been extensively employed in the literature. For each SN in our sample, we fit for M_{Ni} in Equation 4 assuming the t_p and L_p values listed in Table 2. Similar to the procedure of deriving tail M_{Ni} , we run 1000 MC trials to take into account the uncertainties in t_p and L_p when obtaining Arnett M_{Ni} values. Results for individual

SN are provided in Table 2, while basic statistics of both the full Arnett distribution and SESN sub-types are reported in 3. The Arnett M_{Ni} values span $0.04 M_{\odot}$ to $0.67 M_{\odot}$ with a mean value of $0.22 M_{\odot}$. The third panel of Figure 3 displays Arnett M_{Ni} CDFs for different SESN sub-types.

Figure 4 (top panel) presents a comparison between the tail and Arnett M_{Ni} for our sample of SESNe. The results highlight the systematic discrepancy between the two methods. The M_{Ni} values obtained from the radioactive tail modeling are, on average, a factor of ~ 2 smaller than those derived using Arnett's rule. The dashed black line indicates the equality condition between both models. Despite the scatter in the severity of this discrepancy for different SNe, the Arnett model consistently overestimates M_{Ni} for every SESN in our sample. The overestimation of M_{Ni} by Arnett model is also illustrated in Figure 3 (top panel), where the CDF of the Arnett M_{Ni} distribution is below that of the tail distribution with a relatively large margin.

The means and standard deviations of our Arnett-derived M_{Ni} values for different SN types closely match the values reported in Lyman et al. (2016), but our median values are lower than those of Prentice et al. (2016) for Type Ib, Ic, and Ic-BL SNe by $\sim 0.04 M_{\odot}$. This discrepancy is primarily due to different approaches in deriving t_p , which is estimated in Prentice et al. (2016) by measuring the rise time from the half-maximum luminosity to L_p (denoted by $t_{-1/2}$) and using a linear empirical correlation for translating $t_{-1/2}$ to t_p . We also note the Arnett M_{Ni} values of Meza & Anderson (2020) are, on average, 50% lower than our Arnett estimates. This difference can be traced to their anomalously lower peak luminosities as discussed in § 3.5, above.

The inaccuracy of M_{Ni} values obtained from Arnett models has been also shown in several radiative-transfer numerical simulations of SESNe. For example, Dessart et al. (2015, 2016) found that the Arnett's rule overestimated the M_{Ni} of SESNe by 50% and attributed this discrepancy to the fixed electron scattering opacity assumption of Arnett's models. Similarly, Sukhbold et al. (2016) pointed out that Arnett's rule does not hold for their simulations of Type Ib/c SNe evolved from massive single star progenitors. We note that the discrepancy we find between our Arnett

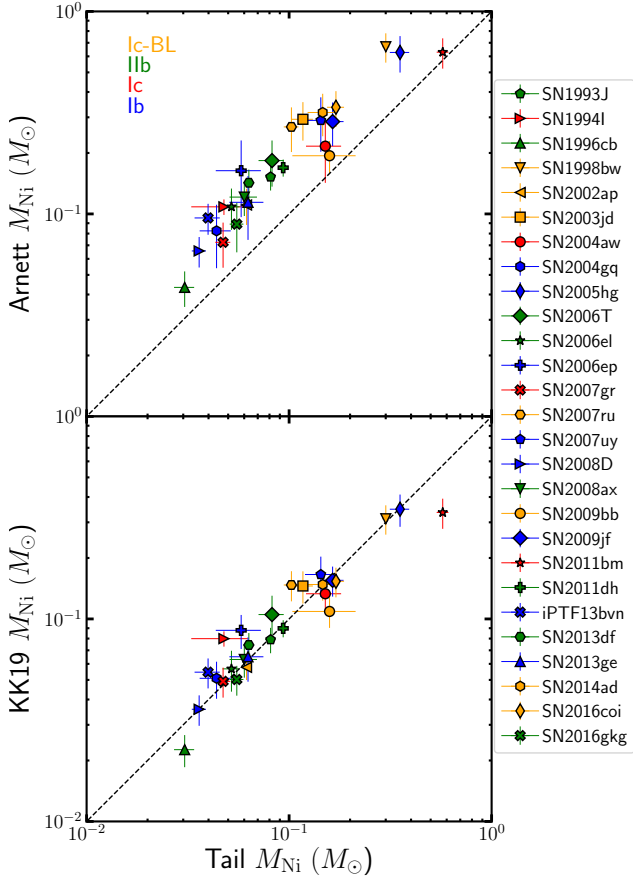


Figure 4. *Top:* M_{Ni} obtained using the radioactive tail modeling (x-axis) and Arnett’s rule (y-axis) for our sample of SESNe. Arnett’s rule yields M_{Ni} values which are systematically a factor of ~ 2 larger. *Bottom:* the same but with M_{Ni} values calculated using the model of KK19 and our empirically-calibrated β values (see § 4.5) displayed on y-axis. Substantially better agreement is found. The markers are color-coded to represent the SESN subtypes with yellow, green, red, and blue indicating SNe Ic-BL, IIb, Ic, and Ib, respectively. The dashed black line denotes equality.

and tail M_{Ni} values is approximately twice as large as that quoted by [Dessart et al. \(2016\)](#).

Despite these limitations, Arnett models have been widely used for deriving M_{Ni} as well as ejecta masses and kinetic energies of SESNe ([Drout et al. 2011](#); [Lyman et al. 2016](#); [Prentice et al. 2016, 2018](#)). A few observational studies have also indicated contrasts between results from modelling the early and late-time light curves of SESNe. For example, [Valenti et al. \(2008\)](#) evoke a “two-zone” model to try to resolve an inconsistency between the explosion parameters derived from early- and late-time light curves of SN2003jd, which they fit with Arnett and radioactive models, respectively. In another study, [Wheeler et al. \(2015\)](#) estimate T_0 values for dozens of SESNe by an analytical relation that depends on M_{ej} and kinetic energy, which were rewritten in terms of the observed rise time and photo-

spheric velocity, assuming Arnett’s model. The estimated T_0 values were found to be in tension with the values measured directly from the light curve tails, which likely is due to the limitations of Arnett’s model. More recently, [Meza & Anderson \(2020\)](#) measured M_{Ni} values for a sample of SESNe using a variety of methods. While their tail M_{Ni} values are lower limits, they confirm that Arnett values are consistently higher than those derived via other methods.

For the rest of our analyses, we assume that our tail M_{Ni} estimates are more realistic than those of the Arnett’s model. This is because the ejecta are expected to be transparent to optical photons over the tail. Therefore, the bolometric luminosity traces the instantaneous heating rate without any further assumption regarding the self-similarity of the energy density profile, which is a fundamental assumption in the Arnett-like models (KK19).

4.3. Comparison of Stripped-Envelope and Type II SN M_{Ni}

As described § 1, by comparing measurements of M_{Ni} for 115 H-rich Type II SNe and 145 SESNe previously published in the literature, [Anderson \(2019\)](#) identified a discrepancy in their distributions, with SESNe displaying a mean M_{Ni} that was a factor of ~ 6 larger than their H-rich counterparts. Subsequently, [Meza & Anderson \(2020\)](#) computed M_{Ni} directly for a smaller sample of SESNe, using a number of methods (Arnett’s rule, KK19, and radioactive tail modeling) in a uniform manner, demonstrating that a statistically significant discrepancy remains. However, the tail M_{Ni} values presented in [Meza & Anderson \(2020\)](#) are strictly lower limits to the true M_{Ni} , as they assume complete trapping of γ -rays, while the Arnett and KK19-based values may each contain systematic biases (in the latter case because they adopt β values which have yet to be observationally calibrated; see § 4.4). Thus, while sufficient to robustly demonstrate that SESN have a different M_{Ni} distribution than Type II SNe, the magnitude of this discrepancy remains somewhat uncertain.

Here, we compare the CDF of M_{Ni} for SESNe derived from our radioactive tail measurements to that for the 115 H-rich Type II SNe from [Anderson \(2019\)](#). M_{Ni} for most of this sample of Type II SNe were calculated using the bolometric luminosity of the radioactive tail of the light curve assuming full trapping of the γ -rays. Figure 5 illustrates the M_{Ni} CDF of our sample of SESNe (orange curve) and the H-rich Type II SNe (green curve). For reference, we also show the original sample M_{Ni} values of SESNe compiled from the literature by [Anderson \(2019\)](#), pink curve)—most of which were obtained using Arnett’s rule—and the lower limits of M_{Ni} from [Meza & Anderson \(2020\)](#), light blue curve). We see that our distribution of M_{Ni} for SESNe measured from the radioactive tail lies between that of the Arnett-based val-

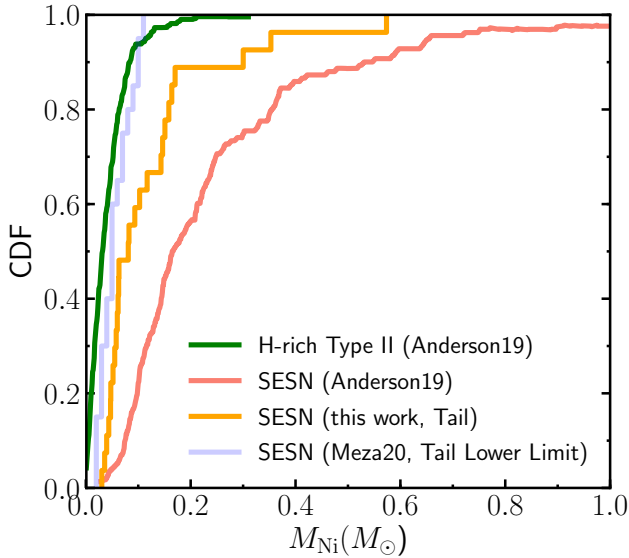


Figure 5. Cumulative Distribution Functions of M_{Ni} for SESN vs. H-rich Type II SNe. The green curve represents tail-based M_{Ni} values for Type II SNe compiled Anderson (2019), while red, light blue and orange curves represent three different distributions for SESNe: the primarily Arnett-based M_{Ni} values compiled from the literature by Anderson (2019), lower limits on tail M_{Ni} computed by Meza & Anderson (2020), and the tail M_{Ni} values derived in § 4. The mean value of the tail-based M_{Ni} values found in this work are a factor of ~ 3 higher than the distribution of Type II SNe.

ues of Anderson (2019) and the tail upper limits of Meza & Anderson (2020), as expected.

Overall we find that our sample of SESNe have a mean value ($\sim 0.12 M_{\odot}$; Table 3) which is a factor of ~ 3 larger than that of H-rich Type II SNe ($\sim 0.044 M_{\odot}$). This is a factor of ~ 2 smaller than the initial discrepancy reported by Anderson (2019) based on Arnett measurements. We conduct K-S tests to the M_{Ni} CDFs of H-rich Type II SNe (Anderson 2019) and SESNe in this work. The test gives D-value = 0.52 and p-value = 10^{-7} , meaning that the CDFs are inconsistent with being drawn from the same distribution. By excluding Type Ic-BL SNe from the test, we find D-value = 0.49 and p-value = 5×10^{-5} , which similarly confirms that Type IIb/Ib/c SNe and H-rich Type II SNe are inconsistent with being drawn from the same distributions.

As in Meza & Anderson (2020) we find that a majority of this discrepancy come from the lack of SESNe in our sample with low M_{Ni} values. The lowest tail M_{Ni} in our sample is $0.03 M_{\odot}$, while an incredible $\sim 48\%$ of Type II SN have M_{Ni} lower than this value. If we recompute the K-S tests described above, but considering only Type II SN with $M_{\text{Ni}} > 0.03 M_{\odot}$, we find a p-value=0.008 for the full sample of SESNe and p-value=0.06 when Type Ic-BL are excluded. This indicates that the sample of IIb/Ib/Ic SNe are marginally consistent with being drawn from the same population as the high M_{Ni} Type II SNe.

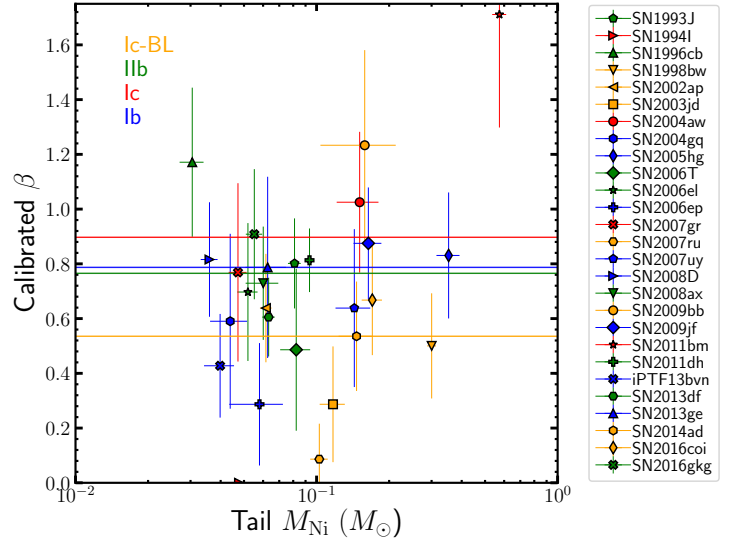


Figure 6. Values for the β parameter given in Equation 6 for the SESNe in our sample, calculated using the observed t_p , L_p , and tail-based M_{Ni} as inputs. The results are color-coded based the SN sub-type. β is a dimensionless parameter defined by KK19 and is correlated with different physical effects such as composition, asymmetries, and the radial extent of ^{56}Ni within ejecta. The horizontal lines indicate the median β value Type IIb (green), Type Ib (green), Type Ic (red), and Type Ic-BL (yellow) SNe.

4.4. Calibration of β values from KK19

In § 4.2 we demonstrated that Arnett-based models yield M_{Ni} values that are a factor of 2 larger than those found from modelling the radioactive tail. While obtaining tail-based M_{Ni} measurements for all SESNe would be ideal, in practice the requisite photometric data exists for only a subset of events. Thus, another means to estimate M_{Ni} from photospheric data alone would be beneficial.

As discussed in § 2, KK19 proposed an analytical model that relates the peak luminosity and its epoch to a general heating function without relying on some of the simplifying assumptions adopted by Arnett's models. This new model, described in Equation 6, depends on a dimensionless parameter β in addition to M_{Ni} , t_p and L_p . KK19 suggested $\beta = 9/8$ for Type Ib/c SNe based on the radiative transfer simulations of SESN light curves from Dessart et al. (2016) and $\beta = 0.82$ for Type IIb/pec SNe based on the observed light curve of SN1987A. However, numerical simulations may not fully represent the behavior of real SESN SNe and the light curve of SN1987A is very different than that of Type IIb SNe. More reliable constraints on β can be obtained from the observed sample of SESNe with independent M_{Ni} values measured from their radioactive tails.

We use Equation 6 to calculate the value of β inferred for each SESN in our sample given their tail M_{Ni} , t_p and L_p provided in Table 2. The uncertainty in the derived β values has contributions from the error in tail M_{Ni} , L_p , and t_p .

Table 4. Table of Derived Parameter Statistics

SN Type	β^*			t_p (days)			Log L_p (erg s $^{-1}$)			f^\dagger			Log fL_p (erg s $^{-1}$)		
	Mean	Median	Std	Mean	Median	Std	Mean	Median	Std	Mean	Median	Std	Mean	Median	Std
IIb	0.78	0.77	0.19	20.2	21.5	2.5	42.37	42.34	0.21	0.24	0.26	0.12	41.87	41.78	0.21
Ib	0.66	0.79	0.21	17.4	16.8	3.0	42.61	42.39	0.30	0.29	0.24	0.10	42.03	41.94	0.29
Ic	0.88	0.90	0.61	17.0	12.7	10.5	42.67	42.67	0.18	0.10	0.13	0.29	41.97	41.62	0.32
Ic-BL	0.56	0.54	0.33	14.4	15.0	2.5	42.87	42.84	0.19	0.32	0.36	0.17	42.49	42.47	0.27
All	0.70	0.70	0.34	17.4	16.6	5.2	42.67	42.55	0.30	0.26	0.29	0.18	42.17	41.94	0.36

* The parameter β is discussed in § 2 and obtained in § 4.4.

† The excess power factor f is defined in § 5.1.5.

In Figure 6 we plot the derived β values versus tail nickel mass for individual SNe. The results exhibit a significant scatter, with β ranging from ≈ 0.0 to 1.7 and a mean value of 0.70 . This is lower, on average, than the $\beta = 9/8$ suggested by KK19 for SESN based on the models of [Dessart et al. \(2016\)](#). This comparison will be examined in more detail in § 4.6. The horizontal lines in Figure 6 indicate the median β value for each SESN sub-type. Table 4 provides summary information on the mean, median and standard deviation of the derived β values for each SN sub-type. The median values of β for Type IIb, Ib, and Ic SNe are roughly similar, but the standard deviation of Type Ic SN is a factor ~ 3 larger due to the small sample size of objects of this type. Type Ic-BL SNe has the smallest median β value of 0.54 , which is $\approx 30\%$ smaller than that of other SESN types.

Two SNe in our sample, SN1994I and SN2007ru, have β close to zero, which may suggest that the derived tail M_{Ni} is inadequate to produce the observed peak luminosity, L_p . Recall that for a fixed M_{Ni} and t_p , a lower β value will yield a higher peak luminosity (see § 2.3). Both of these SNe are fast declining and will be discussed further in § 5.

4.5. Improved Photospheric M_{Ni} Estimates from the Median Calibrated β Values

Using the results from § 4.4 we now assess whether, in practice, the model of KK19 can be used to obtain more reliable M_{Ni} estimates than Arnett for SESNe from photospheric data alone. In Table 2 we list M_{Ni} values for each SN that have been calculated using their observed L_p and t_p in conjunction with the median β value for each SN sub-type listed in Table 4. Errors listed in Table 2 account only for the errors in L_p and t_p and do include the impact of the standard deviation in the distribution of β values. Despite the significant scatter in β values found for individual SNe, we find that the procedure of calculating M_{Ni} assuming the KK19 model and the median β value for each SN sub-type offers a significant improvement over Arnett-based measurements, both for the overall distribution of M_{Ni} values for SESN and for individual objects. These two effects are demonstrated in Figures 3 and 4, respectively.

In the top panel of Figure 3 we present the CDF of M_{Ni} calculated using KK19 with the median calibrated β in comparison to that of the radioactive tail and Arnett methods. As shown, not only is the mean value of the KK19 M_{Ni} distribution the same as that from the radioactive tail measured M_{Ni} (shown by a vertical lines; see also Table 3), but the overall CDF of KK19-measured M_{Ni} values closely approximates that of the radioactive tail M_{Ni} measurements. In the bottom panel of Figure 3 we also display the CDFs of KK19 M_{Ni} estimates separated by SN sub-type. As listed in Table 3, the median values of these distributions are all within $\approx 10\%$ of those calculated from the radioactive tail.

In Figure 4 we demonstrate that this agreement extends to individual objects. The KK19-measured M_{Ni} values for each SNe (bottom panel) are much closer to their tail counterparts compared to the Arnett-derived ones (top panel). We find that, on average, the KK19 M_{Ni} values are within $\sim 17\%$ of the tail-derived values. The largest variations occur for the Type Ic SN 1994I and SN 2011bm for which the nickel mass is overestimated by $\sim 65\%$ and underestimated by $\sim 40\%$, respectively. In contrast, the Arnett-based models systematically over predict M_{Ni} by a factor of ~ 2 (100%) compared to the tail-derived values. We therefore conclude that in cases where the radioactive tail is not observed, the KK19 model with median calibrated β values listed in Table 4 should be used to calculate M_{Ni} for SESN.

4.6. Inferred β Values for Theoretical SESN Light Curves

In addition to providing improved estimates for M_{Ni} from photospheric data alone, the β values calculated for our observed SESNe encode information on the explosion properties and progenitors of the population. Effects such as composition, asymmetry and additional power sources will impact the degree to which the internal energy of the ejecta lags or leads the observed luminosity at the time of peak. In order to assess if the observed population of SESN matches expectations from theory, and to gain insight into the physical processes that dictate β in observed events, we calculate the β values for a set of analytical and numerical light curves models available in the literature.

4.6.1. Arnett Models

First, as a baseline, we derive β for a grid of light curves calculated using an analytic Arnett model. We take t_p and M_{Ni} in the ranges 5–40 days and 0.02 – $0.5 M_{\odot}$, respectively, which correspond to the approximate ranges found for our observed sample. Given a pair of t_p and M_{Ni} , Arnett's rule gives L_p ; we then compute β from Equation 6 using t_p , L_p , and M_{Ni} . The resulting values of β for this grid are plotted as a grey shaded region in Figure 7. As expected given the inconsistency between Arnett and tail-derived nickel masses shown above, these β values are inconsistent with those of our observed population. In particular, the Arnett models occupy a parameter space with high β values in the range of 1.55–1.95, while all but one observed SESN (SN 2011bm) has a calibrated $\beta < 1.25$.

4.6.2. Large Grids of Numerical SESN

Next, we calculate the implied β values for two large suites of simulated SESN light curves from [Dessart et al. \(2016\)](#) and [Ertl et al. \(2019\)](#). Both sets of models consider the explosion of a grid H-poor stars, but utilize different pre-SN stellar structures, explosion assumptions, and hydrodynamic/radiative transfer codes. [Dessart et al. \(2016\)](#) consider a subset of the SN progenitors stripped via close binary interaction that were evolved in [Yoon et al. \(2010\)](#). These models have final pre-explosion masses between 3.0 and $6.5 M_{\odot}$ (initial masses between 16 and $60 M_{\odot}$) and final compositions chosen to span the range of SESN sub-types: Type IIb (defined as $> 50\%$ He plus some residual H in the outer envelope), Type Ib ($\approx 35\%$ He), and Type Ic (H and He deficient). [Dessart et al. \(2016\)](#) uses a piston in order to produce four different explosion energies for each pre-SN structure and also consider two different levels of mixing of radioactive materials. The purpose was to investigate how these physical properties map onto observables, rather than ascertaining what explosion energy and 3D effects would be achieved for a given pre-SN structure a priori. Final SN light curves were calculated with the 1D non-local thermodynamic equilibrium (non-LTE) radiative-transfer code CMFGEN ([Dessart & Hillier 2010](#)), and thus account for time and wavelength-dependent opacity variations.

In contrast, [Ertl et al. \(2019\)](#) consider the explosion of the He star models of [Woosley \(2019\)](#), which are assumed to have lost their H envelopes due to binary interactions prior to the onset of He-ignition, and are evolved to core-collapse in the KEPLER hydrodynamic code ([Weaver et al. 1978](#)). Thus, all pre-SN models are H-deficient, but likely lead to a combination of Type Ib and Type Ic SN, with final surface He mass fractions spanning 0.16 to 0.99. Unlike in [Dessart et al. \(2016\)](#) the SN explosions are carried out in a neutrino-hydrodynamics code P-HOTB ([Janka & Mueller 1996](#)), giving constraints on explosion energies,

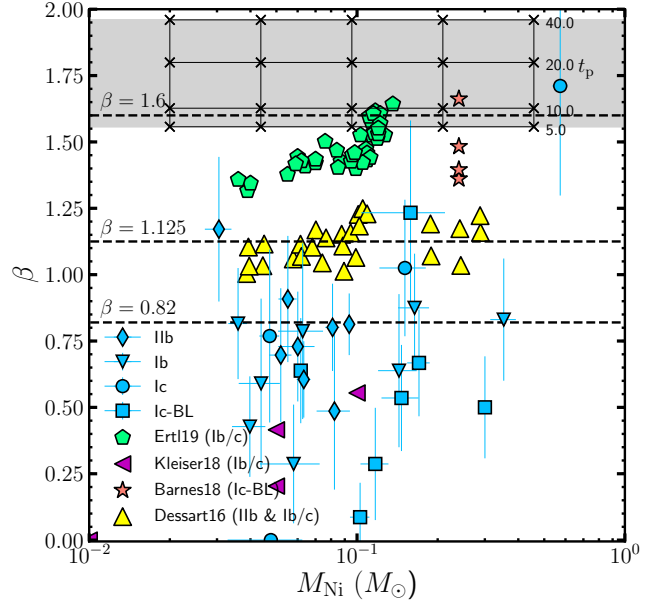


Figure 7. Values for the β parameter given in Equation 6 found for the observed sample of SESNe in comparison to those calculated from a variety of theoretical models. The gray region represents the parameter space that Arnett light curves take for various pairs of t_p and M_{Ni} . The numerical models of [Dessart et al. \(2016\)](#), [Barnes et al. \(2018\)](#), [Kleiser et al. \(2018a,b\)](#), and [Ertl et al. \(2019\)](#) are shown with yellow, red, magenta, and green markers, respectively. The blue markers denote β obtained for our sample of SESNe. The diamond, inverted triangle, circle, and square blue markers represent SN types IIb, Ib, Ic, and Ic-BL, respectively. Overall, the observed population of SESNe possess lower β values with more scatter than the numerical models. Only the models of [Kleiser et al. \(2018a,b\)](#), in which shock cooling contributes a significant fraction of the peak luminosity, overlap with the bulk of the observed population. The horizontal dashed lines represent $\beta = \{0.82, 1.125, 1.6\}$ suggested by KK19 for Type IIb, Ib/c, and Type Ia SNe, respectively.

nickel masses, and remnant masses. The progenitor models that lead to a successful SN have initial He star masses in the range 3.3 – $19.75 M_{\odot}$, which roughly translates to ZAMS mass range of 16 – $51 M_{\odot}$. For these events, bolometric light curves are calculated by post-processing the P-HOTB results in KEPLER. While KEPLER treats electron scattering directly, a constant additive opacity must be adopted to account for the effects of atomic lines. [Ertl et al. \(2019\)](#) chose this ‘line’ opacity to match that of SESN near peak.

For each light curve published in [Dessart et al. \(2016\)](#) and [Ertl et al. \(2019\)](#), we compute β from the published M_{Ni} , t_p , and L_p and Equation 6. The results are presented in Figure 7. The β of [Ertl et al.](#)’s models (green) span the range 1.31–1.64 with more massive initial He stars having relatively higher nickel masses and β values. These are larger than the β values found for all of the models of [Dessart](#)

et al., which are in the range 1.00–1.25 with a mean value of 1.12. Interestingly, the β values of the observed SESNe are considerably smaller and the scatter in the observed β values much larger than those of either set of numerical models. In addition, while the observed SESNe span a similar range of M_{Ni} as the models of Dessart et al. (2016), $\sim 33\%$ have tail-based M_{Ni} higher than any any of the models of Ertl et al. (2019), which were designed to self-consistently determine the radioactive material that can be synthesized by neutrino-driven explosions. We discuss the implications of these results in § 5. For comparison, in Figure 7 we also mark the values $\beta = \{0.82, 1.125, 1.6\}$ that are recommended for Type IIb, Ib/c, and Ia SNe, respectively, by KK19. While $\beta = 0.82$ only slightly overestimates the mean β value of 0.78 obtained for the observed Type IIb SNe, $\beta = 1.125$ substantially overestimates the mean β values for Type Ib and Ic SNe (see Table 4).

4.6.3. Specialized SESN Models

Finally, we also examine the light curve models from two specialized models, which were each designed to probe a specific physical effect that may be present in SESN. Barnes et al. (2018) performs a 2D relativistic hydrodynamic simulation with radiative transport in order to model a single jet-driven explosion. They adopt an analytic pre-SN model with a mass of $3.9 M_{\odot}$ and inject an engine with an engine of $\sim 2 \times 10^{52}$ ergs. The resulting explosion would be classified as a Type Ic-BL, and synthesizes $0.24 M_{\odot}$ of ^{56}Ni . By modelling in multiple dimensions Barnes et al. (2018) find that both the ejecta density profile and distribution of radioactive material are aspherical, and generate light curves for different viewing angles. We compute the β that would be inferred from each of these angles and plot the results as red stars in Figure 7. We find β in the range 1.35–1.65 with models viewed from directions more aligned along the polar axis having progressively higher β . These results lie close to those of the observed Type Ic-BL SN 2009bb ($\beta = 1.23$; $M_{\text{Ni}} = 0.158 M_{\odot}$), but yield significantly larger β values than observed for most of the Type Ic-BL in our sample ($\langle \beta \rangle = 0.56$; see Table 4).

Kleiser et al. (2018a,b) examine the explosion of H-free stars which have either been inflated to large radii or are embedded in a CSM shell ejected shortly before explosion. In both cases, the effective pre-SN radius can be large ($\gtrsim 30 R_{\odot}$) and the subsequent cooling of shock deposited energy can lead to substantial luminosity beyond that provided by ^{56}Ni . Using a combination of the MESA stellar evolution code, hydrodynamic simulations, and the Sedona radiative transport code Kleiser et al. (2018a,b) model the light curves that would result from the explosion of such systems, finding luminosities of $\log L = 41.2\text{--}42.5$ on timescales of 10–20 days. Originally proposed as a means

to explain the class of rapidly evolving Type I SN (e.g. SN2010X; Kasliwal et al. 2010), a majority of the models of Kleiser et al. (2018a,b) are computed without contributions from ^{56}Ni . However, Kleiser et al. (2018a) also provide six fiducial models in which they add 0.01, 0.05, and $0.1 M_{\odot}$ of ^{56}Ni to one of their models with two levels of mixing. We calculate β for the three “strongly” mixed models—which yield relatively smooth, as opposed to strongly double-peaked, light curve morphologies most similar to observed Type Ib/c SN—and plot the results in Figure 7 (magenta triangles). We find β values of $\sim 0.0\text{--}0.55$, which overlap with the *lower* end of observed SESNe. Implications of these results are discussed below.

5. DISCUSSION

In the sections above, we calculated ^{56}Ni masses for 27 SESNe based on their late-time tails. We confirm that these masses are systematically lower than those derived by Arnett-like analytical models. These masses allow us to *observationally* calibrate the β value introduced in KK19 based on their observed rise times and peak luminosities. Despite scatter, we demonstrate that calculating M_{Ni} using the medians of our empirically calibrated β values offers a significantly improved estimation when only photospheric light curve data is available. However, in doing so we find that (a) the β values inferred for SESNe are systematically lower than those found from most numerical simulations of SESN explosions and (b) a systematic discrepancy remains between the ^{56}Ni masses for SESNe and Type II core-collapse SNe. In the sections below, we discuss the possible origins for each of these discrepancies, and their implications for the progenitors and explosion mechanism of stripped envelope core-collapse SN.

5.1. Possible Origins of Low β Values

In § 4.6, we presented the β values inferred for different numerical models of SESNe. The results show that most numerical models give higher β values compared to observations. In order to disentangle the origin of this discrepancy, in Figure 8 we present the pairwise dependence and histograms of the three quantities that determine β , i.e., L_p , t_p , and M_{Ni} , for both the numerical models detailed in § 4.6 and observed SESNe. This figure illustrates that:

1. While both the observed sample and model SESN show a correlation between M_{Ni} and L_p , the observed objects exhibit considerably ($\sim 0.3\text{--}0.4$ dex) larger peak luminosities for a given M_{Ni} .
2. The observed SESNe tend to have shorter rise times compared to the models. The median rise time for the entire sample is 16.6 days, as compared to 19.5 and 26.8 days for the Ertl et al. (2019) and Dessart et al. (2016) models, respectively.

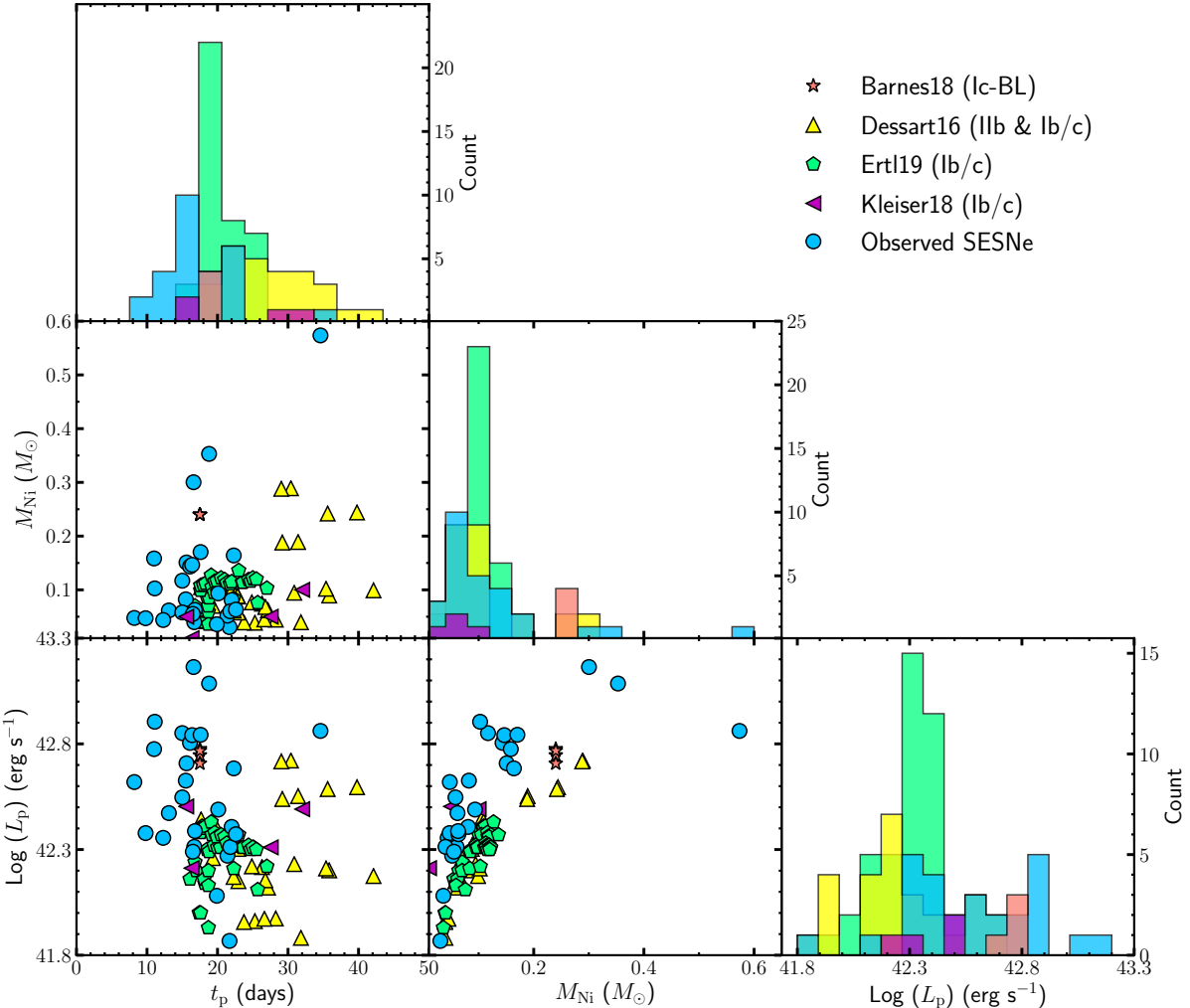


Figure 8. Pairwise relationship of $\log L_p$, t_p , and M_{Ni} for numerical models of Dessart et al. (2016) (yellow upper triangles), Barnes et al. (2018) (red stars), Kleiser et al. (2018a,b) (magenta left triangles), Ertl et al. (2019) (green pentagons) and our sample of SESNe (blue circles). Diagonal panels display the histogram of the three parameters. M_{Ni} for the observed sample are those derived from modelling the late-time tail (§ 4.1). Overall the observed population of SESNe display shorter rise times and have substantially higher peak luminosities for a given M_{Ni} than the numerical models.

As described in § 2.3 both rise time and peak luminosity are *inversely* proportional to β . Thus, shorter rise times would primarily act to *increase* β . Indeed, it appears that the main driver between the different β values of the Ertl et al. (2019) and Dessart et al. (2016) models is that Ertl et al. find shorter rise times for a given M_{Ni} . This effect was discussed in Ertl et al. (2019) and is primarily due to their adoption of a constant line opacity. In contrast, the higher luminosity for a given M_{Ni} would act to lower β , and this is therefore likely the origin of the discrepancy in β displayed in Figure 7. Here we investigate the possible physical origins of this discrepancy, as well as the scatter in effective β displayed by the observed sample.

5.1.1. Dark Period

The light curves of some SESNe are expected to have a “dark period” between the explosion epoch and the first

observable light if they lack prominent cooling envelope emission and their ^{56}Ni is deposited deep within the ejecta (Piro & Nakar 2013). This dark period is roughly the time that takes for the diffusion front to move inward (in a Lagrangian sense) and reach the shallowest regions of the ejecta that contain ^{56}Ni . KK19 use numerical simulations to show that for a completely central heating source, the dark period could be as large as 20 days, while the models of Dessart et al. (2016) typically have dark periods $\lesssim 5$ days.

While the explosion epochs for many of the Type IIB SN in our sample were determined by the presence of cooling envelope emission, it is possible other events may possess a non-negligible dark period. This would have two primary effects on our analysis: (i) our current rise times would be underestimated as the explosion would occur earlier than a power-law fit to the light curves implies and (ii) our current

tail-based nickel masses would be underestimated as the $^{56}\text{Ni} \rightarrow ^{56}\text{Co} \rightarrow ^{56}\text{Fe}$ decay chain would need to reproduce the same tail luminosity at a longer time post-explosion. Both effects could alleviate some of the discrepancies between the observed and model SESN in Figure 8.

To quantify the effect of a possible dark period on our analysis in § 4, we increase the rise time by 5 days and recompute both tail M_{Ni} and β for our sample of SESNe. The results show that, on average, the tail M_{Ni} values would increase by $\sim 14\%$, while the inferred β values would actually further *decrease* by $\sim 8\%$ compared to those listed in Table 2. We therefore conclude that while a dark period could explain some of the discrepancy between the rise times of observed SESNe and numerical models, the subsequent increase in inferred M_{Ni} is insufficient to offset this effect, and an even larger discrepancy between the β of the observed SESNe and numerical models would result.

5.1.2. Composition, Opacity, and Recombination

Composition can influence the morphology of SESN light curves, primarily through its influence on the opacity of the ejecta. In practice, the opacity will also depend both on the age of the SN and the spatial location of the diffusion front, as effects such as ionization, recombination, and line blanketing will modify the opacity compared to constant pure electron scattering. Notably, while ionized, the opacity of a given material will be dominated by electron scattering and will subsequently fall to significantly once recombined (e.g. KK19, Piro & Morozova 2014). KK19 investigate the impact of ion recombination on light curve rise times, peak luminosities and β values for ejecta with varying compositions. For ejecta with higher recombination temperatures, the opacity will fall at an earlier time. This leads to a shorter dark period, shorter observed rise time, and higher peak luminosity, which combine to yield a *lower* β value. KK19 find that for a central heating source and ejecta with recombination temperatures of ~ 12000 K, 6000 K, and 4000 K (appropriate for He, H, and C/O compositions, respectively), β values of 0.70, 0.94, and 1.12 result. $\beta = 0.7$ also corresponds to the mean value found for our observed SESN sample (see Table 4). Thus, it may be possible to reconcile all of the (i) short rise times (ii) high peak luminosities and (iii) low β values of the observed SESN sample if the ^{56}Ni is primarily diffusing through *He-rich* ejecta. However, we note that the models Dessart et al. (2016) which include full non-LTE radiation transport and wavelength dependent opacities, all display β around 1.12, despite the fact that over 60% of their models have compositions that are $> 50\%$ He. This implies that the ^{56}Ni synthesized in the explosions is primarily diffusing through the denser CO cores, whose opacities remain high long after the He envelopes. In this case, the surface He would have

recombined at earlier times and would be effectively transparent near maximum light, consistent with the low black-body temperatures observed for many SESN near maximum (~ 9000 K; Piro & Morozova 2014).

Thus, given that all SESN progenitors will possess a CO core, the effects of He recombination can likely only explain the low β values of observed SESN if a significant fraction of their M_{Ni} is mixed out into a He-rich envelope. The models of Dessart et al. (2016) currently implement two mixing schemes. Thus, stronger or more directed mixing, such as that described in Hammer et al. (2010), may be required. However, while such effects may reconcile observations of some Type I Ib and Ib SNe, it is unclear if they can similarly explain the trends observed in Type Ic and Ic-BL SNe—which also display low β values, but do not have any detectable He in their spectra. While the presence of He in the progenitors of Type Ic SN is still debated (e.g. Hachinger et al. 2012), arguments rely on the He being transparent. Mixing of ^{56}Ni into a He envelope would significantly increase the likelihood of non-thermal excitation and thus observed spectroscopic features, making this explanation less plausible (Dessart et al. 2012).

5.1.3. Mixing of Radioactive Material

The mixing of radioactive material within SN ejecta is generally difficult to model due to its inherent 3D nature (e.g. Joggerst et al. 2009; Hammer et al. 2010; Wongwathanarat et al. 2015). While it is generally believed that the ^{56}Ni distribution of SESN is more centrally concentrated than in Type Ia SN, there is also evidence that at least some mixing is required to reproduce SESNe observations (Dessart et al. 2012). The distribution of ^{56}Ni inside the ejecta can alter the shape of the light curve and thus impact the β parameter. In particular, for smoothly stratified models, more extended ^{56}Ni distributions (corresponding to stronger mixing) will lead to both shorter rise times and higher luminosities for a given M_{Ni} (e.g. Dessart et al. 2016, KK19). However, KK19 find that these two effects combine to produce a *higher* β value for more strongly mixed models. They find that the lowest β that can be achieved for a constant opacity model is $\beta = 4/3$ for a centrally concentrated heating source. Thus, while mixing of radioactive elements can modify the rise time and luminosity of SNe, it is likely that these would need to be coupled with the composition and opacity effects described in § 5.1.2 to explain the low β values of the observed SESNe.

5.1.4. Asymmetry

There is growing evidence from a combination of spectropolarimetry, nebular spectroscopy, and resolved SN remnants that some SESN may be asymmetric (e.g. Valenti et al. 2011; Milisavljevic & Fesen 2015; Tanaka 2017). As

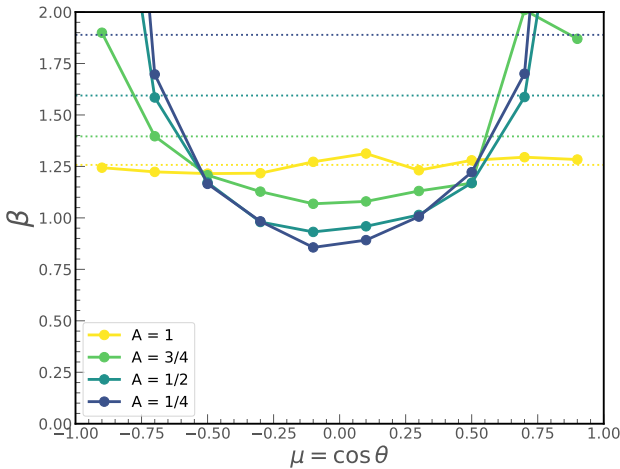


Figure 9. Inferred value of β for the set of 2D radiative transfer models, depending on viewing angle $\mu = \cos\theta$, where $\mu = \pm 1$ corresponds to the pole and $\mu = 0$ corresponds to the equator. Different lines correspond to model ejecta with varying axis ratios $A = v_r/v_z$ (i.e. degree of asymmetry), where $A = 1$ (yellow line) corresponds to a spherically symmetric ejecta. Dashed horizontal lines indicate the inferred β when averaged over all viewing angles. We find that while line-of-site effects can lead to significant scatter in observed β , asymmetry will *increase* the average β found for a population.

shown in Figures 7 and 8, the β values of the mildly asymmetric simulations of Barnes et al. (2018) depend on the observer's viewing angle. This is primarily due to a variations in the observed peak luminosity, with viewing angles with larger L_p leading to lower β values. Thus, depending on their nature, asymmetries in ^{56}Ni mixing or ejecta distribution can be reflected both in the mean value and scatter in the β parameters observed for a population of SESNe.

To test the degree to which asymmetry can modify observed β values for a population, we run a set of light curve simulations with varying degrees of ejecta asymmetry using the multi-dimensional radiative transfer code Sedona (Kasen et al. 2006). We assume an axisymmetric homologously expanding ejecta profile consisting of a broken power-law in density following Chevalier & Soker (1989) and Kasen et al. (2016). To account for deviations from spherical symmetry, we vary the semi-major axis as in Darbha & Kasen (2020) parameterized by $A \equiv v_r/v_z$, where v_r and v_z are the outer ejecta velocities at the equator and pole, respectively. In total, we run four radiative transfer simulations with $A \leq 1$, i.e., prolate ejecta configurations.

We choose fiducial values of $M_{\text{ej}} = 2 M_{\odot}$, $v_z = 10^4 \text{ km s}^{-1}$ for our simulations. To account for the heating, we set the innermost $0.1 M_{\odot}$ to consist of ^{56}Ni . Finally, we assume a constant grey opacity of $\kappa = 0.2 \text{ cm}^2 \text{ g}^{-1}$. The resulting

light curve is then calculated at ten different viewing angles $\mu = \cos\theta$, in the range $\mu \in \{-1, 1\}$, where $\mu = 0$ and $\mu = \pm 1$ view the ejecta along the equator and poles, respectively.

We measure the different values of $L_p(\mu, A)$ and $t_p(\mu, A)$ for the output bolometric light curves, which we then map onto an inferred β based on Equation 6 and the model parameter $M_{\text{Ni}} = 0.1 M_{\odot}$. In Figure 9, we show the inferred values of β for the different set of asymmetric ejecta configurations and viewing angles. As expected, β does not vary with viewing angle for the case $A = 1$, i.e. no ejecta asymmetry. However, increasing the degree of asymmetry results in lower inferred β when viewed along the equator, and higher β when viewed at the poles. This is due to L_p being larger when viewed along the equator, where the projected surface area is largest; similarly, L_p is decreased along the poles for asymmetric ejecta due to a smaller projected surface area (Darbha & Kasen 2020). This is in agreement with the results found in Barnes et al. (2018).

While the total spread in β values observed for our asymmetric simulations is $\gtrsim 1$ —well matched to the scatter in our observed population—when averaged over all viewing angles, we find that *asymmetry acts to increase the mean inferred value of β* . This is opposite to the direction that has been observed, where the average β is systematically *lower* than the spherically symmetric models of Dessart et al. (2016); Ertl et al. (2019) (as well as the $A = 1$ model run in this work). Thus, insofar as asymmetry can be represented by an expanding broken power-law ellipsoid, we conclude that asymmetry, although possibly explaining some of the scatter seen in Figure 7, cannot explain the *systematically lower* inferred values of β . However, we note that when asymmetry is strong other effects such as the development of non-radial flows (Matzner et al. 2013; Afsariardchi & Matzner 2018) and the ejection of nickel-rich clumps to high velocities (Drout et al. 2016) could further influence the light curve morphology.

5.1.5. Additional Power Sources

In § 5.1 we demonstrated that the main driver of the low β values for our observed SESNe was their high L_p for a given M_{Ni} (Figure 8). Thus, another plausible explanation for the origin of the discrepancy between the β distribution of the models and the observed SESNe is that additional power sources beyond the radioactive decay of ^{56}Ni contribute to the peak luminosity of SESNe. This was previously proposed by Ertl et al. (2019), who noted that their numerical simulations were unable to reproduce the brighter half of observed Type Ib/c SNe luminosity function (Figure 8). In addition, when modeling a sample of SESNe with the luminosity integral method of Katz et al. (2013), Sharon & Kushnir (2020) required an additional model parameter, which they interpret as non-negligible amount of emission pro-

duced by power sources beyond ^{56}Ni . The presence of an additional luminosity source near peak could also explain why the observed SESNe show an even larger discrepancy between Arnett and tail-measured M_{Ni} than the theoretical models of [Dessart et al. \(2016\)](#).

Within our sample, the need for additional power sources is particularly conceivable for SN 1994I and SN 2007ru, for which we derived a negative and close to zero β , respectively. In practice, a negative β is not physical in the general definition given by KK19 (see Equation 5). Rather, this implies that the version of this equation which assumes pure ^{56}Ni heating (Equation 6) is *incapable* of producing such a bright peak luminosity on the observed rise time when coupled with the M_{Ni} measured from the radioactive tail. While these are the most extreme cases, other observed SESNe may also have extra power sources contributing to the observed luminosity. In this case, attributing the observed peak luminosity solely to the radioactive decay of ^{56}Ni will result in smaller β values than expected based on their composition and ^{56}Ni distribution.

Besides the radioactive decay of ^{56}Ni , power sources that can contribute to the light curves of CCSN include shock cooling emission, ejecta interaction with circumstellar material (CSM), and energy from a central engine. Here, we assess the viability of each of these sources in explaining the discrepancy between observed and model SESNe, and implications thereof.

Luminosity Required: We begin by evaluating how much excess luminosity would be required to reconcile the β values we derive in § 4.4 with those of the theoretical models in § 4.6. To do so, we assume that the average value of $\beta=1.125$ found by the models of [Dessart et al. \(2016\)](#) is accurate for SESNe powered only by radioactive decay. Given their full treatment of radiative transfer-opacity, this is equivalent to assuming that the composition, energetics, and mixing of radioactive material included in [Dessart et al. \(2016\)](#) reflect reality. Then, using $\beta=1.125$, the M_{Ni} and t_p listed in Table 2, and Equation 6, we calculate the luminosity that ^{56}Ni decay can produce at the peak time of the SN. From this, we define an “excess luminosity factor”, f , as the fraction of peak luminosity that is in excess over what is expected from a $\beta=1.125$ explosion with a nickel mass as defined by the light curve tail.

The resulting values of f for each SN are listed in Table 2 and the mean, median and standard deviation in Table 4. In Figure 10 we plot the excess luminosity factor, f , versus the excess luminosity, $f \times L_p$. We emphasize that these “excess luminosity” values should be taken as order of magnitude estimates only, as they (a) neglect any variations from $\beta=1.125$ that can be caused by effects such as enhanced nickel mixing and asymmetry and (b) inherently assume that the radioactive component peaks at the same time as

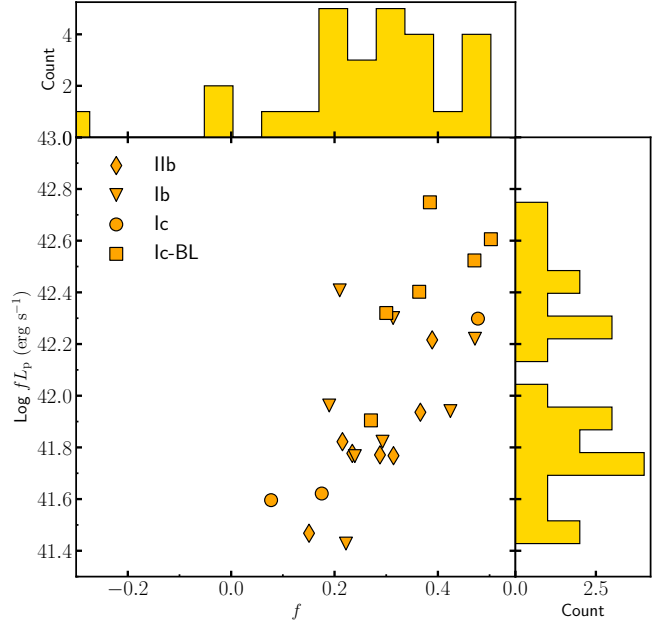


Figure 10. Excess power factor, f , versus logarithm of excess peak luminosity $f L_p$ for our SESNe sample. Histograms of f and $f L_p$ are displayed on x- and y-axis, respectively. Overall we find that reconciling the observed SESNe with current numerical simulations would require 7–50% of their peak luminosity to come from power sources other than ^{56}Ni . This corresponds to excess luminosities of $41.4 \lesssim \log(f L_p) \lesssim 42.8$.

the observed light curve; depending on the nature of the excess luminosity source this need not be the case. Nevertheless, they provide a useful diagnostic.

Overall, we find f values in the range of -0.33 to 0.5 . Three events (SN 1996cb, SN2009bb, and SN 2010bm) have negative f values, reflecting the fact that they had measured $\beta > 1.125$, and thus do not *require* additional power sources. For the remaining 24 events, we find that if the models of [Dessart et al. \(2016\)](#) and our tail M_{Ni} are accurate, we require that ~ 7 – 50% of the their peak luminosities come from sources other than ^{56}Ni . This translates into considerable excess luminosity in the range of 2.5×10^{41} – 5.5×10^{42} erg s^{-1} or, equivalently, peak bolometric magnitudes for the excess power source of $-14.9 \text{ mag} > M_{\text{bol}} > -18.2 \text{ mag}$. Out of the 6 events that would require the most excess luminosity, five are Type Ic-BL, while the events which require the highest *fraction* of the peak luminosity to come from other sources, are mixed between sub-types.

Shock Cooling and CSM Interaction: Both shock cooling and CSM interaction face challenges in explaining this required excess emission. First, shock cooling emission is predicted to be both faint and short-lived for the compact progenitors ($R \sim R_{\odot}$) typically evoked for H-poor SESNe ([Nakar & Sari 2010; Rabinak & Waxman 2011](#)). Second, the substantial luminosity required and lack of narrow emission lines in the majority of SESNe spectra limit any poten-

tial CSM to dense and confined shell or disk-like configurations (Chevalier & Irwin 2011; Moriya & Tominaga 2012; Smith et al. 2015), which are not predicted from standard models of stellar evolution (Smith 2014). However, recent progress may change this picture: models show that particularly low mass He stars ($\lesssim 3 M_{\odot}$) can undergo substantial inflation (achieving radii $\gtrsim 100 R_{\odot}$; e.g. Yoon et al. 2010, Kleiser et al. 2018a, Woosley 2019) and there is increasing observational evidence that many CCSN—of all varieties—undergo a period of enhanced mass loss shortly before core-collapse (e.g Margutti et al. 2015; Drout et al. 2016; Bruch et al. 2020). Thus, a significant fraction of SESN progenitors may have large effective radii ($\gtrsim 20 R_{\odot}$) in which case shock deposited energy can contribute substantially to their observed luminosity.

As described in § 4.6.3, Kleiser et al. (2018a,b) model the light curves that would result solely from the diffusion of shock deposited energy in both of these scenarios. The set of O/He-rich CSM shells modeled in Kleiser et al. (2018b) have masses of $1-4 M_{\odot}$ and are located at radii of $\sim 15-60 R_{\odot}$, designed to mimic an intense final mass-loss episode. They find transients which rise to peak magnitudes of $-15 \text{ mag} < M_r < -18 \text{ mag}$ on timescales of $\sim 8-25$ days—parameters which are exceptionally well matched to our estimates above for the excess luminosity required. Indeed, as shown in Figure 7, when a small amount of ^{56}Ni is added, the models of Kleiser et al. (2018a,b) are able to reproduce the low β values of the observed population.

While the particular theoretical models plotted in Figure 7 show slight double-peaked morphology in their *optical* light curves—which are not typically observed—they were created by adding ^{56}Ni to a shock cooling curve that reaches -17 mag and contributes $\gtrsim 50\%$ of the luminosity near peak. In contrast, we expect the SESN in our sample to still be dominated by the radioactive decay of ^{56}Ni , with a median excess luminosity factor of $f = 0.29$. In addition, a number of Type Ib/c SNe, show evidence for multiple emission components when observed early in the u-band/UV, with SN 2013ge also exhibiting *narrow* high-velocity absorption features, which may be indicative of a shell-like CSM structure (Drout et al. 2016; Kleiser et al. 2018b). However, the lack of *prominent* double-peaked structure in many Type Ib/c SNe combined with the need for excess luminosity near maximum light implies that: (i) the He/O-rich material which leads to the large effective radius cannot be too tenuous, in which case it would become optically thin on a timescale of \sim days (Dessart et al. 2018; Woosley 2019) and (ii) the ^{56}Ni synthesized in the explosion must be well-mixed to avoid a significant dark-period and subsequently large offset in time between the two emission components (Kleiser et al. 2018b).

We therefore conclude that shock cooling emission is a viable source for the excess luminosity required to reconcile SESN observations and models. While low mass He stars can reach the radii required through “natural” stellar evolution processes, such events are predicted to eject very little radioactive ^{56}Ni (Kleiser et al. 2018a; Woosley 2019). Thus, reproducing the full observed population via this mechanism likely requires a significant number of SESN to undergo intense late-stage mass loss due to instabilities (Smith & Arnett 2014; Woosley 2019), internal gravity waves (Quataert & Shiode 2012; Fuller & Ro 2018), or some other physical process during the final nuclear burning stages. We emphasize that this shock cooling emission will rapidly fade once the ejecta cools to the recombination temperature of O/He-rich material ($t < 40$ days), and thus M_{Ni} measured at >60 days post-explosion should be unaffected.

Central Engines: On the other hand, a central engine could provide the additional energy source required to power the light curve around peak. We note, in particular, that we found a lower mean β value and require a higher mean excess luminosity for Type Ic-BL SNe (Table 4), for which central engines are commonly evoked. Both magnetars and collapsars can provide a natural source of extra luminosity, in the form of spin-down energy and fallback accretion (Dexter & Kasen 2013), respectively. Ertl et al. (2019) investigate the former as a power source for SESNe in general, arguing that even the formation of a more moderate millisecond pulsar (e.g. Yoon et al. 2010) may be sufficient for rotational energy to impact the SN light curve without impacting the overall energetics.

We use the magnetar spin-down energy and timescale of Kasen (2017) together with SN timescale and ejecta velocity of Kasen et al. (2016) to estimate the general phase space of magnetar properties required to provide the excess luminosity found above. In Figure 11 we plot rise time vs. excess luminosity for our sample of SESNe. Also shown are lines which represent the peak luminosity and time achieved by magnetar models with a fixed period but varying magnetic field (solid) and fixed magnetic field but varying periods (dotted). All models assume an opacity of $\kappa = 0.1 \text{ cm}^2 \text{ g}^{-1}$, explosion energy of 10^{51} erg , and were calculated both for $M_{\text{ej}} = 2 M_{\odot}$ (top panel) and $M_{\text{ej}} = 5 M_{\odot}$ (bottom panel)—chosen to span the range of SESNe ejecta masses from Lyman et al. (2016). For $M_{\text{ej}} = 2 M_{\odot}$, P values of $10-116 \text{ ms}$ and $B_{14} (= B/10^{14} \text{ G})$ values of $7-59$ are yield luminosities consistent with requirements. For $M_{\text{ej}} = 5 M_{\odot}$, similar magnetic field strengths but shorter periods are necessary with $P = 2-32 \text{ ms}$ and $B_{14} = 10-60$ spanning the phase space occupied by most SESNe in our sample. The ranges of P and B_{14} found here overlap with—but extend to longer periods and higher mag-

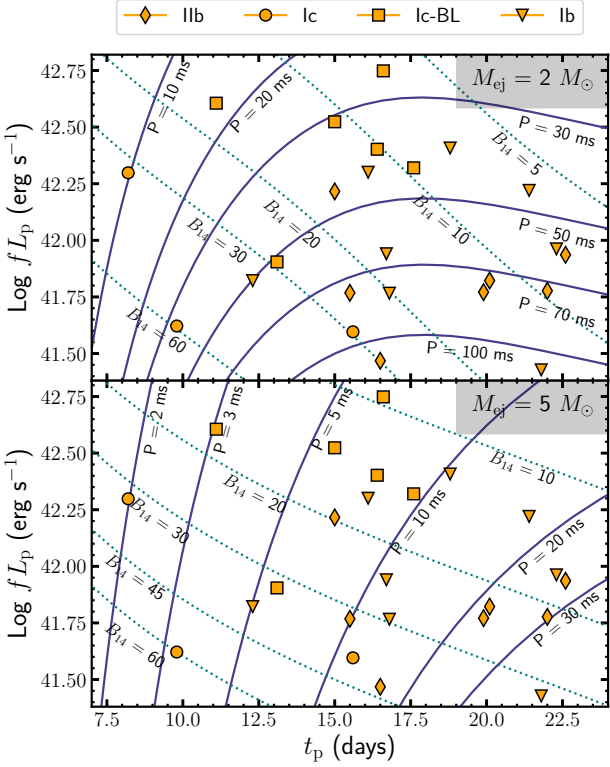


Figure 11. Logarithm of excess peak luminosity $\log(f L_p)$ versus peak time t_p for our sample of SESNe (excluding SNe with negative excess factor f). The diamond, inverted triangle, circle, and square orange markers represent SN types IIb, Ib, Ic, and Ic-BL, respectively. Also plotted are lines which represent the peak luminosity and time achieved by magnetar spin-down models with a fixed period but varying magnetic field strength (solid purple) and fixed magnetic field but varying periods (dotted cyan) for ejecta mass of $2 M_\odot$ (top panel) and $5 M_\odot$ (bottom panel).

netic field strengths—than those of magnetar fits to super-luminous SN light curves by Nicholl et al. (2017).

Figure 12 displays two representative magnetar models for the excess peak luminosity of SN2008ax. The excess emission factor is 0.29, corresponding to a luminosity of $5.90 \times 10^{41} \text{ erg s}^{-1}$ (dashed line). The blue curve illustrates a model with $B_{14} = 36$, $P = 32 \text{ ms}$, and $M_{\text{ej}} = 5 M_\odot$, while the orange curve represents a magnetar with $B_{14} = 19$, $P = 116 \text{ ms}$, and $M_{\text{ej}} = 2 M_\odot$. Both models peak at the level of the excess luminosity calculated above, but have different magnetar properties and light curve morphologies. Figure 12 highlights that, unlike shock cooling emission, if a magnetar contributes to the light curve near peak it can also power a non-negligible portion of the tail luminosity. In this case, tail-based measurement of M_{Ni} would be overestimated and, as a result, the fraction of the peak luminosity which must come from sources other than radioactive decay *underestimated*. While we find that fits over 60–120 days post-explosion, as performed in § 3.5, are

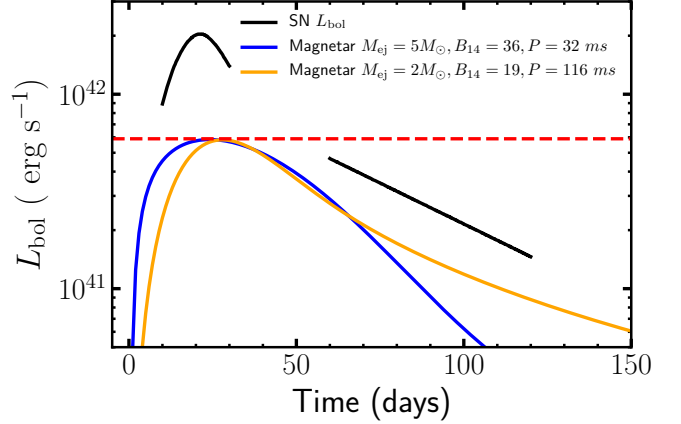


Figure 12. The bolometric light curve of SN2008ax in comparison with two magnetar models. The dashed red horizontal line indicates the excess emission in the L_p of SN2008ax (i.e., $\sim 29\%$ of the peak luminosity). If this power is contributed to the light curve by sources other than the radioactive decay, then β increases to the same level as predicted by numerical models, i.e., $\beta \simeq 1.125$, shown in Figure 7. The orange and blue curves represent the light curves of two magnetar models with the peak time and luminosity similar to the t_p and $0.29 \times L_p$ of SN2008ax.

not sufficient to distinguish between the $L(t) \propto t^{-2}$ power-law decline of the magnetar model and the exponential form of the radioactive decay of ^{56}Ni (Equation 1) future modelling of a subset of SESNe with data covering a longer baseline ($\gtrsim 200$ days) could potentially break this degeneracy. If the slope of the tail is shallower than $^{56}\text{Co} \rightarrow ^{56}\text{Fe}$ conversion rate this could also be an indication that other power sources are contributing to the light curve tail (e.g., Ertl et al. 2019). However, none of the SESNe in our sample have such a shallow tail.

5.1.6. Possible Limitations of Tail M_{Ni} Values

Throughout the analyses of § 4 and § 5, and specifically in the model comparisons of Figures 7 and 8, we assume that the M_{Ni} values measured from radioactive decay modeling of SESNe light curve tails are reliable estimates for the actual M_{Ni} . In § 2 we utilize the tail luminosity model of Wygoda et al. (2019), which relies on a number of assumptions. In particular, the simple scaling form of the γ -ray deposition factor, $f_{\text{dep}} = 1 - e^{-(t/T_0)^{-2}}$, only holds if the ejecta is in homologous expansion and if the γ -ray opacity is constant and purely absorptive. However, both are standard assumptions: ejecta should reach a phase of homologous expansion after several expansion doubling times—i.e., a few days—while we measure M_{Ni} over epoches > 60 days, and the γ -ray opacity is typically assumed to be constant (Sutherland & Wheeler 1984; Clocchiatti & Wheeler 1997; Wygoda et al. 2019). We note that other assumptions on the ejecta density distribution or nickel mixing will

chiefly change pre-factors of T_0 , while the scaling relation of f_{dep} —and therefore M_{Ni} —will remain unchanged.

Thus, we conclude that any error in M_{Ni} is due to the late-time *luminosity* that we attribute to radioactive decay not being accurate. This could occur if either the bolometric corrections utilized in § 3.5 do not adequately describe the behavior of our observed sample or if power sources other than radioactive decay (e.g., CSM interaction, magnetar spin down; see above) contribute to the luminosity on the light curve tail. In the latter case, our tail M_{Ni} values would be overestimated. However, we emphasize that this effect can not resolve the tension with theoretical models shown in Figures 7 and 8. Rather, lower M_{Ni} values would *increase* the discrepancy, with the observed sample of SESNe showing even larger L_p values for a given M_{Ni} .

5.2. Consequences of M_{Ni} Discrepancy with Type II SNe

The discrepancy in ^{56}Ni mass distributions for SESNe and Type II SN was first identified using Arnett-based measurements of M_{Ni} for SESNe (Anderson 2019). In § 4.2 we demonstrated that Arnett’s rule over-predicts M_{Ni} for SESNe by roughly a factor of 2—likely due to both to limitations in Arnett’s model (KK19) and to possible contributions from additional power sources to the peak luminosity of SESN (§ 5.1.5). However, in § 4.3 we find that even when tail-based M_{Ni} values are used, our population of SESNe have a mean M_{Ni} value ($0.12 M_{\odot}$) which is a factor of ~ 3 higher than Type II SNe ($0.044 M_{\odot}$). Therefore a critical question remains: what makes the M_{Ni} distribution of SESNe skew to larger values than Type II SNe? Are the M_{Ni} values for the *observed* population of SESNe biased? If not, does the discrepancy with Type II SNe come about because SNe originate from higher ZAMS mass stars? Or are the ZAMS masses of SESNe and H-rich Type II SNe are somewhat similar, but other physical mechanisms are responsible for the observed difference in the M_{Ni} distribution? Here, we consider each of these questions in turn.

Does the distribution of M_{Ni} derived accurately represent the true distribution of M_{Ni} synthesized in the core-collapse of H-poor stars? As highlighted by Meza & Anderson (2020), the discrepancy between SESNe and Type II SNe is primarily due to a *lack* of observed SESNe with low M_{Ni} . While the light curves of Type II SNe—powered predominately by H recombination—remain luminous for $\gtrsim 100$ days regardless of M_{Ni} , low- M_{Ni} SESN may be faint and/or rapidly-evolving. In particular, as described in § 5.1.5, low-mass stripped He stars ($M \lesssim 3-4 M_{\odot}$; corresponding to ZAMS $\lesssim 12-15 M_{\odot}$) can inflate to large radii prior to core-collapse. Stars with these initial masses likely dominate the population of Type II SNe, due to the initial mass function. However, the explosion of their stripped counterparts may be dominated by bright and rapidly-fading cooling envelope

emission (Dessart et al. 2018; Kleiser et al. 2018a; Woosley 2019), with minimal contributions from ^{56}Ni . Observationally, these could manifest as rapidly-fading Type I SN (Kasliwal et al. 2010; Drout et al. 2013), Type Ibn SNe (Hosseinzadeh et al. 2017), or the broader class of fast blue optical transients (Drout et al. 2014) rather than “traditional” SESNe. Such events were not explicitly included in our sample, and have rarely been followed to late enough times to constrain the M_{Ni} ejected. While the rates of rapidly-evolving transients ($\sim 4-7\%$ of the CCSN rate; Drout et al. 2014) are not sufficient to fully resolve the discrepancy, they could reduce its significance.

Alternatively, the M_{Ni} distribution shown in Figure 5 may not accurately represent reality if the light curves of SESNe are not solely powered by the radioactive decay of ^{56}Ni and the timescale of the additional power source(s) is $\gtrsim 60$ days (see § 5.1.5). In this case, attributing the full tail luminosity to ^{56}Ni would lead to an overestimate of the true values. Within this context, it is notable that while simulations of neutrino-driven core-collapse SNe (Sukhbold et al. 2016; Ertl et al. 2019) are able to self-consistently produce the range of M_{Ni} values observed in H-rich Type II SN ($\sim 0.004-0.13 M_{\odot}$; Müller et al. 2017, Afsariardchi et al. 2019), they are unable to produce M_{Ni} values as high as those derived for the upper $\sim 30\%$ of our SESN sample (see Figures 7 and 8). It was for this reason that Ertl et al. (2019) invoked magnetars to explain the observed light curves of SESNe. While this may resolve the M_{Ni} discrepancy, it subsequently requires that magnetars influence SESN at a higher rate than Type II SNe. This may be a natural consequence of stripped stars retaining a larger fraction of their angular momentum, which in H-rich stars is lost primarily due to rotational breaking when the star expands to the RSG phase (e.g., Ertl et al. 2019).

Do SESNe originate from higher ZAMS mass stars than Type II SNe? If observational biases cannot explain the relative lack of low M_{Ni} SESNe, the discrepancy could indicate that SESNe preferentially form from higher ZAMS mass stars—which are expected to synthesize higher amounts of M_{Ni} —than Type II SNe. While on face value this may favor the single star progenitor channel, this is in tension with the observed occurrence rate of SESNe, which is much higher than the explosion rate of stars with ZAMS mass $\gtrsim 25 M_{\odot}$ that eventually become WR stars (Smith et al. 2011). In addition, the mass-loss rate of massive stars is still uncertain, and it is not clear whether all massive stars with ZAMS mass $\gtrsim 25 M_{\odot}$ can strip their H envelope (Smith 2014). Another possible explanation is that SESNe do form stripped binaries and span the same *overall* ZAMS masses as Type II SNe. However, while the relative rates of Type II SNe are dominated by the IMF, SESNe are skewed to higher relative masses. This may be a natural consequence of the

close binary fraction being larger for high mass stars (Moe & Di Stefano 2017; Moe et al. 2019), although detailed population synthesis calculations are necessary to test this hypothesis. We note that the population of SESNe coming from a distribution skewed to higher ZAMS masses, and hence shorter lifetimes, would be consistent with the fact that they are found closer, on average, to sites of active star formation than Type II SNe (Anderson et al. 2012).

Do additional physical mechanisms modify the M_{Ni} synthesized in SESNe? Alternatively, if the M_{Ni} distribution for SESNe is accurate, and SESNe originate from similar ZAMS masses as H-rich Type II SNe, then there must be some physical processes that make the M_{Ni} of SESNe larger. While it is often assumed stripping of the H and even He envelope via binary interaction should leave the inner core structure of the primary star intact (e.g., Fryer & Kalogera 2001)—in which case the M_{Ni} distributions of SESNe and Type II SNe should be indistinguishable—this picture may not be complete. In particular:

- (i) In close binaries, fast orbital rotation, tides, magnetic breaking, and angular momentum transport can influence the convective core sizes profoundly (e.g., Song et al. 2018). Therefore, changes in the core structure may impact the M_{Ni} production.
- (ii) A fraction of SESNe may originate from the merger of binary stars (Zapartas et al. 2017). In this case, a more massive core capable of producing a larger amount of ^{56}Ni may result. Although the rate of this merger channel seems to be relatively small ($\sim 12\%$ of SESNe; Zapartas et al. 2017), it will boost the overall M_{Ni} of SESNe produced via the binary channel.

Additional analysis is required to distinguish the contributions of each of the above scenarios towards explaining the discrepancy in observed M_{Ni} for H-poor and H-rich core-collapse SNe.

6. SUMMARY AND CONCLUSIONS

In this paper we measure the ^{56}Ni masses for a sample of 27 stripped-envelope core-collapse SNe with well-constrained explosion epochs and late-time photometric coverage by modeling their radioactive tails. We both compare these results to Arnett-based M_{Ni} measurements and use them, in conjunction with the observed rise times and peak luminosities for the sample, to *observationally* calibrate the β parameter in the new analytic light curve model of Khatami & Kasen (2019). This parameter β allows the internal energy of the ejecta to lag or lead the observed luminosity at the time of peak (in contrast to Arnett models), and is hence a function of the ejecta composition, mixing, asymmetry, and total power sources. Here we summarize our main conclusions.

1. We find ^{56}Ni masses for measured from the radioactive tail of $0.03 M_{\odot} < M_{\text{Ni}} < 0.57 M_{\odot}$, with a median value of $0.08 M_{\odot}$. Type Ic-BL SNe show higher M_{Ni} on average, with a median value of $0.15 M_{\odot}$.
2. M_{Ni} values measured via Arnett's rule are systematically larger than those found from the radioactive tail by a factor of ~ 2 . While limitations in Arnett's rule when applied to SESNe had previously been discussed, this discrepancy is approximately a factor of 2 larger than that found in recent numerical simulations (Dessart et al. 2016).
3. Using our observed rise times, peak luminosities, and tail-based M_{Ni} values we find KK19 β values which range from $0.0 < \beta < 1.71$, with a median value of 0.70. The calibrated β values show significant spread with a standard deviation of 0.34. Two objects exhibit $\beta \approx 0$, which may indicate that the radioactive decay of ^{56}Ni is incapable of powering their entire peak luminosity.
4. Despite the observed scatter, we demonstrate that using the model of KK19 with the median values of our calibrated β (see Table 4) yields significantly improved measurements of M_{Ni} in comparison to Arnett's rule when only photospheric data is available.
5. When comparing our calibrated β values to those of inferred from a range numerical light curve models (e.g. Dessart et al. 2016; Ertl et al. 2019), we find that the simulations significantly overestimate β , on average. This is primarily due to the observed sample displaying dramatically larger (~ 0.3 – 0.4 dex) peak luminosities for a given M_{Ni} than the numerical models. The observed population also exhibits shorter rise times, on average.
6. We investigate a number of physical mechanisms to explain this observed discrepancy. Effects due to composition and the mixing of radioactive elements can lead to brighter peak luminosities and shorter rise times while the impact of line-of-sight variations due to explosion asymmetries can lead the observed scatter in β . However, all of these mechanisms have difficulties explaining systematically low β values for the entire population.
7. Alternatively, we demonstrate that the discrepancy with numerical models can be resolved if an additional power source contributes between ~ 7 – 50% of the peak luminosity of SESNe; corresponding to luminosities in the range of 2.5×10^{41} – 5.5×10^{42} erg s^{-1} . Both diffusion of shock deposited energy and magnetar spin-down are capable of providing the required luminosity over appropriate timescales.

8. Finally, we demonstrate that recently identified discrepancy between the observed M_{Ni} distribution of SESNe and H-rich Type II SNe (Anderson 2019; Meza & Anderson 2020) persists in our sample. The median tail M_{Ni} value of our SESNe is a factor of ~ 3 higher than those of Type II SNe. We discuss several explanations for this discrepancy including that low M_{Ni} SESN may primarily manifest as rapidly evolving transients as opposed to “traditional” SESN, that the close binary fraction increases for higher mass stars leading to SESN forming from a distribution of ZAMS masses skewed relative to the IMF, and that additional physical effects may impact the M_{Ni} production in SESNe.

ACKNOWLEDGMENTS

We thank Daniel Kasen, Katelyn Breivik, and Jennifer Hoffman for helpful comments and discussions, Tuguldur Sukhbold for providing numerical simulation results and Siva Darbha for providing code used to setup the 2D radiative transfer models.

M.R.D. acknowledges support from the Natural Sciences and Engineering Research Council (NSERC) of

Canada through a Discovery Grant (RGPIN-2019-06186), the Canada Research Chairs Program, the Canadian Institute for Advanced Research (CIFAR), and the Dunlap Institute at the University of Toronto. This research benefited from interactions made possible by the Gordon on Betty Moore Foundation through grant GBMF5076.

D.K.K. is supported by the National Science Foundation Graduate Research Fellowship Program. This research used resources of the National Energy Research Scientific Computing Center, a DOE Office of Science User Facility supported by the Office of Science of the U.S. Department of Energy under Contract No. DE-AC0205CH11231.

D.S.M. was supported in part by a Leading Edge Fund from the Canadian Foundation for Innovation (project No.30951) and a Discovery Grant (RGPIN-2019-06524) from the Natural Sciences and Engineering Research Council (NSERC) of Canada.

REFERENCES

Afsariardchi, N., & Matzner, C. D. 2018, *ApJ*, 856, 146, doi: [10.3847/1538-4357/aab3d4](https://doi.org/10.3847/1538-4357/aab3d4)

Afsariardchi, N., Moon, D.-S., Drouot, M. R., et al. 2019, *ApJ*, 881, 22, doi: [10.3847/1538-4357/ab2be6](https://doi.org/10.3847/1538-4357/ab2be6)

Anderson, J. P. 2019, *A&A*, 628, A7, doi: [10.1051/0004-6361/201935027](https://doi.org/10.1051/0004-6361/201935027)

Anderson, J. P., Habergham, S. M., James, P. A., & Hamuy, M. 2012, *MNRAS*, 424, 1372, doi: [10.1111/j.1365-2966.2012.21324.x](https://doi.org/10.1111/j.1365-2966.2012.21324.x)

Antilogus, P., Gilles, S., Pain, R., et al. 2006, *The Astronomer’s Telegram*, 854, 1

Arnett, W. D. 1980, *ApJ*, 237, 541, doi: [10.1086/157898](https://doi.org/10.1086/157898)

—. 1982, *ApJ*, 253, 785, doi: [10.1086/159681](https://doi.org/10.1086/159681)

Barnes, J., Duffell, P. C., Liu, Y., et al. 2018, *ApJ*, 860, 38, doi: [10.3847/1538-4357/aabf84](https://doi.org/10.3847/1538-4357/aabf84)

Begelman, M. C., & Sarazin, C. L. 1986, *ApJL*, 302, L59, doi: [10.1086/184637](https://doi.org/10.1086/184637)

Bersten, M. C., Folatelli, G., García, F., et al. 2018, *Nature*, 554, 497, doi: [10.1038/nature25151](https://doi.org/10.1038/nature25151)

Bianco, F. B., Modjaz, M., Hicken, M., et al. 2014, *ApJS*, 213, 19, doi: [10.1088/0067-0049/213/2/19](https://doi.org/10.1088/0067-0049/213/2/19)

Bruch, R. J., Gal-Yam, A., Schulze, S., et al. 2020, *arXiv e-prints*, arXiv:2008.09986. <https://arxiv.org/abs/2008.09986>

Cao, Y., Kasliwal, M. M., Arcavi, I., et al. 2013, *ApJL*, 775, L7, doi: [10.1088/2041-8205/775/1/L7](https://doi.org/10.1088/2041-8205/775/1/L7)

Chevalier, R. A., & Irwin, C. M. 2011, *ApJL*, 729, L6, doi: [10.1088/2041-8205/729/1/L6](https://doi.org/10.1088/2041-8205/729/1/L6)

Chevalier, R. A., & Soker, N. 1989, *ApJ*, 341, 867, doi: [10.1086/167545](https://doi.org/10.1086/167545)

Clocchiatti, A., & Wheeler, J. C. 1997, *ApJ*, 491, 375, doi: [10.1086/304961](https://doi.org/10.1086/304961)

Clocchiatti, A., Wheeler, J. C., Benetti, S., & Frueh, M. 1996, *ApJ*, 459, 547, doi: [10.1086/176919](https://doi.org/10.1086/176919)

Colgate, S. A., & McKee, C. 1969, *ApJ*, 157, 623, doi: [10.1086/150102](https://doi.org/10.1086/150102)

Darbha, S., & Kasen, D. 2020, *arXiv e-prints*, arXiv:2002.00299. <https://arxiv.org/abs/2002.00299>

Dessart, L., & Hillier, D. J. 2010, *MNRAS*, 405, 2141, doi: [10.1111/j.1365-2966.2010.16611.x](https://doi.org/10.1111/j.1365-2966.2010.16611.x)

Dessart, L., Hillier, D. J., Li, C., & Woosley, S. 2012, *MNRAS*, 424, 2139, doi: [10.1111/j.1365-2966.2012.21374.x](https://doi.org/10.1111/j.1365-2966.2012.21374.x)

Dessart, L., Hillier, D. J., Woosley, S., et al. 2015, *MNRAS*, 453, 2189, doi: [10.1093/mnras/stv1747](https://doi.org/10.1093/mnras/stv1747)

—. 2016, *MNRAS*, 458, 1618, doi: [10.1093/mnras/stw418](https://doi.org/10.1093/mnras/stw418)

Dessart, L., Yoon, S.-C., Livne, E., & Waldman, R. 2018, *A&A*, 612, A61, doi: [10.1051/0004-6361/201732363](https://doi.org/10.1051/0004-6361/201732363)

Dexter, J., & Kasen, D. 2013, *ApJ*, 772, 30, doi: [10.1088/0004-637X/772/1/30](https://doi.org/10.1088/0004-637X/772/1/30)

Drout, M. R., Soderberg, A. M., Gal-Yam, A., et al. 2011, *ApJ*, 741, 97, doi: [10.1088/0004-637X/741/2/97](https://doi.org/10.1088/0004-637X/741/2/97)

Drout, M. R., Soderberg, A. M., Mazzali, P. A., et al. 2013, *ApJ*, 774, 58, doi: [10.1088/0004-637X/774/1/58](https://doi.org/10.1088/0004-637X/774/1/58)

Drout, M. R., Chornock, R., Soderberg, A. M., et al. 2014, *ApJ*, 794, 23, doi: [10.1088/0004-637X/794/1/23](https://doi.org/10.1088/0004-637X/794/1/23)

Drout, M. R., Milisavljevic, D., Parrent, J., et al. 2016, *ApJ*, 821, 57, doi: [10.3847/0004-637X/821/1/57](https://doi.org/10.3847/0004-637X/821/1/57)

Eldridge, J. J., Fraser, M., Smartt, S. J., Maund, J. R., & Crockett, R. M. 2013, *MNRAS*, 436, 774, doi: [10.1093/mnras/stt1612](https://doi.org/10.1093/mnras/stt1612)

Eldridge, J. J., Izzard, R. G., & Tout, C. A. 2008, *MNRAS*, 384, 1109, doi: [10.1111/j.1365-2966.2007.12738.x](https://doi.org/10.1111/j.1365-2966.2007.12738.x)

Eldridge, J. J., & Maund, J. R. 2016, *MNRAS*, 461, L117, doi: [10.1093/mnrasl/slw099](https://doi.org/10.1093/mnrasl/slw099)

Ertl, T., Woosley, S. E., Sukhbold, T., & Janka, H. T. 2019, arXiv e-prints, arXiv:1910.01641. <https://arxiv.org/abs/1910.01641>

Filippenko, A. V. 1997, *ARA&A*, 35, 309, doi: [10.1146/annurev.astro.35.1.309](https://doi.org/10.1146/annurev.astro.35.1.309)

Folatelli, G., Van Dyk, S. D., Kuncarayakti, H., et al. 2016, *ApJL*, 825, L22, doi: [10.3847/2041-8205/825/2/L22](https://doi.org/10.3847/2041-8205/825/2/L22)

Fremling, C., Sollerman, J., Taddia, F., et al. 2016, *A&A*, 593, A68, doi: [10.1051/0004-6361/201628275](https://doi.org/10.1051/0004-6361/201628275)

Fryer, C. L., & Kalogera, V. 2001, *ApJ*, 554, 548, doi: [10.1086/321359](https://doi.org/10.1086/321359)

Fuller, J., & Ro, S. 2018, *MNRAS*, 476, 1853, doi: [10.1093/mnras/sty369](https://doi.org/10.1093/mnras/sty369)

Galama, T. J., Vreeswijk, P. M., van Paradijs, J., et al. 1998, *Nature*, 395, 670, doi: [10.1038/27150](https://doi.org/10.1038/27150)

Gerke, J. R., Kochanek, C. S., Prieto, J. L., Stanek, K. Z., & Macri, L. M. 2011, *ApJ*, 743, 176, doi: [10.1088/0004-637X/743/2/176](https://doi.org/10.1088/0004-637X/743/2/176)

Guillochon, J., Parrent, J., Kelley, L. Z., & Margutti, R. 2017, *ApJ*, 835, 64, doi: [10.3847/1538-4357/835/1/64](https://doi.org/10.3847/1538-4357/835/1/64)

Hachinger, S., Mazzali, P. A., Taubenberger, S., et al. 2012, *MNRAS*, 422, 70, doi: [10.1111/j.1365-2966.2012.20464.x](https://doi.org/10.1111/j.1365-2966.2012.20464.x)

Hammer, N. J., Janka, H. T., & Müller, E. 2010, *ApJ*, 714, 1371, doi: [10.1088/0004-637X/714/2/1371](https://doi.org/10.1088/0004-637X/714/2/1371)

Hosseinzadeh, G., Arcavi, I., Valenti, S., et al. 2017, *ApJ*, 836, 158, doi: [10.3847/1538-4357/836/2/158](https://doi.org/10.3847/1538-4357/836/2/158)

Hunter, J. D. 2007, *Computing in Science and Engineering*, 9, 90, doi: [10.1109/MCSE.2007.55](https://doi.org/10.1109/MCSE.2007.55)

Janka, H. T., & Mueller, E. 1996, *A&A*, 306, 167

Joggerst, C. C., Woosley, S. E., & Heger, A. 2009, *ApJ*, 693, 1780, doi: [10.1088/0004-637X/693/2/1780](https://doi.org/10.1088/0004-637X/693/2/1780)

Jordi, K., Grebel, E. K., & Ammon, K. 2006, *A&A*, 460, 339, doi: [10.1051/0004-6361:20066082](https://doi.org/10.1051/0004-6361:20066082)

Kasen, D. 2017, *Unusual Supernovae and Alternative Power Sources*, ed. A. W. Alsabti & P. Murdin, 939, doi: [10.1007/978-3-319-21846-5_32](https://doi.org/10.1007/978-3-319-21846-5_32)

Kasen, D., Metzger, B. D., & Bildsten, L. 2016, *ApJ*, 821, 36, doi: [10.3847/0004-637X/821/1/36](https://doi.org/10.3847/0004-637X/821/1/36)

Kasen, D., Thomas, R. C., & Nugent, P. 2006, *ApJ*, 651, 366, doi: [10.1086/506190](https://doi.org/10.1086/506190)

Kasliwal, M. M., Kulkarni, S. R., Gal-Yam, A., et al. 2010, *ApJL*, 723, L98, doi: [10.1088/2041-8205/723/1/L98](https://doi.org/10.1088/2041-8205/723/1/L98)

Katz, B., Kushnir, D., & Dong, S. 2013, arXiv e-prints, arXiv:1301.6766. <https://arxiv.org/abs/1301.6766>

Khatami, D. K., & Kasen, D. N. 2019, *ApJ*, 878, 56, doi: [10.3847/1538-4357/ab1f09](https://doi.org/10.3847/1538-4357/ab1f09)

Kim, H.-J., Yoon, S.-C., & Koo, B.-C. 2015, *ApJ*, 809, 131, doi: [10.1088/0004-637X/809/2/131](https://doi.org/10.1088/0004-637X/809/2/131)

Kleiser, I., Fuller, J., & Kasen, D. 2018a, *MNRAS*, 481, L141, doi: [10.1093/mnras/sly180](https://doi.org/10.1093/mnras/sly180)

Kleiser, I. K. W., Kasen, D., & Duffell, P. C. 2018b, *MNRAS*, 475, 3152, doi: [10.1093/mnras/stx3321](https://doi.org/10.1093/mnras/stx3321)

Li, W., Leaman, J., Chornock, R., et al. 2011, *MNRAS*, 412, 1441, doi: [10.1111/j.1365-2966.2011.18160.x](https://doi.org/10.1111/j.1365-2966.2011.18160.x)

Lyman, J. D., Bersier, D., & James, P. A. 2014, *MNRAS*, 437, 3848, doi: [10.1093/mnras/stt2187](https://doi.org/10.1093/mnras/stt2187)

Lyman, J. D., Bersier, D., James, P. A., et al. 2016, *MNRAS*, 457, 328, doi: [10.1093/mnras/stv2983](https://doi.org/10.1093/mnras/stv2983)

Margutti, R., Guidorzi, C., Lazzati, D., et al. 2015, *ApJ*, 805, 159, doi: [10.1088/0004-637X/805/2/159](https://doi.org/10.1088/0004-637X/805/2/159)

Matzner, C. D., Levin, Y., & Ro, S. 2013, *ApJ*, 779, 60, doi: [10.1088/0004-637X/779/1/60](https://doi.org/10.1088/0004-637X/779/1/60)

Maund, J. R. 2018, *MNRAS*, 476, 2629, doi: [10.1093/mnras/sty093](https://doi.org/10.1093/mnras/sty093)

McKenzie, E. H., & Schaefer, B. E. 1999, *PASP*, 111, 964, doi: [10.1086/316404](https://doi.org/10.1086/316404)

McQuinn, K. B. W., Skillman, E. D., Dolphin, A. E., Berg, D., & Kennicutt, R. 2016, *ApJ*, 826, 21, doi: [10.3847/0004-637X/826/1/21](https://doi.org/10.3847/0004-637X/826/1/21)

—. 2017, *AJ*, 154, 51, doi: [10.3847/1538-3881/aa7aad](https://doi.org/10.3847/1538-3881/aa7aad)

Meza, N., & Anderson, J. P. 2020, arXiv e-prints, arXiv:2002.01015. <https://arxiv.org/abs/2002.01015>

Milisavljevic, D., & Fesen, R. A. 2015, *Science*, 347, 526, doi: [10.1126/science.1261949](https://doi.org/10.1126/science.1261949)

Modjaz, M., Blondin, S., Kirshner, R. P., et al. 2014, *AJ*, 147, 99, doi: [10.1088/0004-6256/147/5/99](https://doi.org/10.1088/0004-6256/147/5/99)

Moe, M., & Di Stefano, R. 2017, *ApJS*, 230, 15, doi: [10.3847/1538-4365/aa6fb6](https://doi.org/10.3847/1538-4365/aa6fb6)

Moe, M., Kratter, K. M., & Badenes, C. 2019, *ApJ*, 875, 61, doi: [10.3847/1538-4357/ab0d88](https://doi.org/10.3847/1538-4357/ab0d88)

Morales-Garoffolo, A., Elias-Rosa, N., Benetti, S., et al. 2014, *MNRAS*, 445, 1647, doi: [10.1093/mnras/stu1837](https://doi.org/10.1093/mnras/stu1837)

Moriya, T. J., & Tominaga, N. 2012, *ApJ*, 747, 118, doi: [10.1088/0004-637X/747/2/118](https://doi.org/10.1088/0004-637X/747/2/118)

Müller, T., Prieto, J. L., Pejcha, O., & Clocchiatti, A. 2017, *ApJ*, 841, 127, doi: [10.3847/1538-4357/aa72f1](https://doi.org/10.3847/1538-4357/aa72f1)

Nakar, E., & Sari, R. 2010, *ApJ*, 725, 904, doi: [10.1088/0004-637X/725/1/904](https://doi.org/10.1088/0004-637X/725/1/904)

Nicholl, M., Guillochon, J., & Berger, E. 2017, *ApJ*, 850, 55, doi: [10.3847/1538-4357/aa9334](https://doi.org/10.3847/1538-4357/aa9334)

Pandey, S. B., Anupama, G. C., Sagar, R., et al. 2003, *MNRAS*, 340, 375, doi: [10.1046/j.1365-8711.2003.06148.x](https://doi.org/10.1046/j.1365-8711.2003.06148.x)

Pastorello, A., Kasliwal, M. M., Crockett, R. M., et al. 2008, *MNRAS*, 389, 955, doi: [10.1111/j.1365-2966.2008.13618.x](https://doi.org/10.1111/j.1365-2966.2008.13618.x)

Pignata, G., Stritzinger, M., Soderberg, A., et al. 2011, *ApJ*, 728, 14, doi: [10.1088/0004-637X/728/1/14](https://doi.org/10.1088/0004-637X/728/1/14)

Piro, A. L., & Morozova, V. S. 2014, *ApJL*, 792, L11, doi: [10.1088/2041-8205/792/1/L11](https://doi.org/10.1088/2041-8205/792/1/L11)

Piro, A. L., & Nakar, E. 2013, *ApJ*, 769, 67, doi: [10.1088/0004-637X/769/1/67](https://doi.org/10.1088/0004-637X/769/1/67)

Podsiadlowski, P., Joss, P. C., & Hsu, J. J. L. 1992, *ApJ*, 391, 246, doi: [10.1086/171341](https://doi.org/10.1086/171341)

Prentice, S. J., Mazzali, P. A., Pian, E., et al. 2016, *MNRAS*, 458, 2973, doi: [10.1093/mnras/stw299](https://doi.org/10.1093/mnras/stw299)

Prentice, S. J., Ashall, C., Mazzali, P. A., et al. 2018, *MNRAS*, 478, 4162, doi: [10.1093/mnras/sty1223](https://doi.org/10.1093/mnras/sty1223)

Qiu, Y., Li, W., Qiao, Q., & Hu, J. 1999, *AJ*, 117, 736, doi: [10.1086/300731](https://doi.org/10.1086/300731)

Quataert, E., & Shiode, J. 2012, *MNRAS*, 423, L92, doi: [10.1111/j.1745-3933.2012.01264.x](https://doi.org/10.1111/j.1745-3933.2012.01264.x)

Rabinak, I., & Waxman, E. 2011, *ApJ*, 728, 63, doi: [10.1088/0004-637X/728/1/63](https://doi.org/10.1088/0004-637X/728/1/63)

Richmond, M. W., Treffers, R. R., Filippenko, A. V., & Paik, Y. 1996a, *AJ*, 112, 732, doi: [10.1086/118048](https://doi.org/10.1086/118048)

Richmond, M. W., Treffers, R. R., Filippenko, A. V., et al. 1994, *AJ*, 107, 1022, doi: [10.1086/116915](https://doi.org/10.1086/116915)

Richmond, M. W., van Dyk, S. D., Ho, W., et al. 1996b, *AJ*, 111, 327, doi: [10.1086/117785](https://doi.org/10.1086/117785)

Riess, A. G., Macri, L. M., Hoffmann, S. L., et al. 2016, *ApJ*, 826, 56, doi: [10.3847/0004-637X/826/1/56](https://doi.org/10.3847/0004-637X/826/1/56)

Sahu, D. K., Anupama, G. C., Chakradhari, N. K., et al. 2018, *MNRAS*, 475, 2591, doi: [10.1093/mnras/stx3212](https://doi.org/10.1093/mnras/stx3212)

Sahu, D. K., Gurugubelli, U. K., Anupama, G. C., & Nomoto, K. 2011, *MNRAS*, 413, 2583, doi: [10.1111/j.1365-2966.2011.18326.x](https://doi.org/10.1111/j.1365-2966.2011.18326.x)

Sahu, D. K., Tanaka, M., Anupama, G. C., Gurugubelli, U. K., & Nomoto, K. 2009, *ApJ*, 697, 676, doi: [10.1088/0004-637X/697/1/676](https://doi.org/10.1088/0004-637X/697/1/676)

Sana, H., de Mink, S. E., de Koter, A., et al. 2012, *Science*, 337, 444, doi: [10.1126/science.1223344](https://doi.org/10.1126/science.1223344)

Schlafly, E. F., & Finkbeiner, D. P. 2011, *ApJ*, 737, 103, doi: [10.1088/0004-637X/737/2/103](https://doi.org/10.1088/0004-637X/737/2/103)

Sharon, A., & Kushnir, D. 2020, arXiv e-prints, arXiv:2004.07244. <https://arxiv.org/abs/2004.07244>

Shivvers, I., Modjaz, M., Zheng, W., et al. 2017, *PASP*, 129, 054201, doi: [10.1088/1538-3873/aa54a6](https://doi.org/10.1088/1538-3873/aa54a6)

Shivvers, I., Filippenko, A. V., Silverman, J. M., et al. 2019, *MNRAS*, 482, 1545, doi: [10.1093/mnras/sty2719](https://doi.org/10.1093/mnras/sty2719)

Smartt, S. J., Eldridge, J. J., Crockett, R. M., & Maund, J. R. 2009, *MNRAS*, 395, 1409, doi: [10.1111/j.1365-2966.2009.14506.x](https://doi.org/10.1111/j.1365-2966.2009.14506.x)

Smith, N. 2014, *ARA&A*, 52, 487, doi: [10.1146/annurev-astro-081913-040025](https://doi.org/10.1146/annurev-astro-081913-040025)

Smith, N., & Arnett, W. D. 2014, *ApJ*, 785, 82, doi: [10.1088/0004-637X/785/2/82](https://doi.org/10.1088/0004-637X/785/2/82)

Smith, N., Li, W., Filippenko, A. V., & Chornock, R. 2011, *MNRAS*, 412, 1522, doi: [10.1111/j.1365-2966.2011.17229.x](https://doi.org/10.1111/j.1365-2966.2011.17229.x)

Smith, N., Mauerhan, J. C., Cenko, S. B., et al. 2015, *MNRAS*, 449, 1876, doi: [10.1093/mnras/stv354](https://doi.org/10.1093/mnras/stv354)

Song, H. F., Meynet, G., Maeder, A., et al. 2018, *A&A*, 609, A3, doi: [10.1051/0004-6361/201731073](https://doi.org/10.1051/0004-6361/201731073)

Sravan, N., Marchant, P., & Kalogera, V. 2019, *ApJ*, 885, 130, doi: [10.3847/1538-4357/ab4ad7](https://doi.org/10.3847/1538-4357/ab4ad7)

Stritzinger, M. D., Taddia, F., Burns, C. R., et al. 2018, *A&A*, 609, A135, doi: [10.1051/0004-6361/201730843](https://doi.org/10.1051/0004-6361/201730843)

Sukhbold, T., Ertl, T., Woosley, S. E., Brown, J. M., & Janka, H.-T. 2016, *ApJ*, 821, 38, doi: [10.3847/0004-637X/821/1/38](https://doi.org/10.3847/0004-637X/821/1/38)

Sutherland, P. G., & Wheeler, J. C. 1984, *ApJ*, 280, 282, doi: [10.1086/161995](https://doi.org/10.1086/161995)

Tanaka, M. 2017, *Philosophical Transactions of the Royal Society of London Series A*, 375, 20160273, doi: [10.1098/rsta.2016.0273](https://doi.org/10.1098/rsta.2016.0273)

Taubenberger, S., Pastorello, A., Mazzali, P. A., et al. 2006, *MNRAS*, 371, 1459, doi: [10.1111/j.1365-2966.2006.10776.x](https://doi.org/10.1111/j.1365-2966.2006.10776.x)

Tsvetkov, D. Y., Volkov, I. M., Sorokina, E., et al. 2012, *Peremennye Zvezdy*, 32, 6. <https://arxiv.org/abs/1207.2241>

Utrobin, V. P., Wongwathanarat, A., Janka, H. T., & Müller, E. 2017, *ApJ*, 846, 37, doi: [10.3847/1538-4357/aa8594](https://doi.org/10.3847/1538-4357/aa8594)

Valenti, S., Benetti, S., Cappellaro, E., et al. 2008, *MNRAS*, 383, 1485, doi: [10.1111/j.1365-2966.2007.12647.x](https://doi.org/10.1111/j.1365-2966.2007.12647.x)

Valenti, S., Fraser, M., Benetti, S., et al. 2011, *MNRAS*, 416, 3138, doi: [10.1111/j.1365-2966.2011.19262.x](https://doi.org/10.1111/j.1365-2966.2011.19262.x)

Valenti, S., Taubenberger, S., Pastorello, A., et al. 2012, *ApJL*, 749, L28, doi: [10.1088/2041-8205/749/2/L28](https://doi.org/10.1088/2041-8205/749/2/L28)

Van Dyk, S. D., de Mink, S. E., & Zapartas, E. 2016, *ApJ*, 818, 75, doi: [10.3847/0004-637X/818/1/75](https://doi.org/10.3847/0004-637X/818/1/75)

Van Dyk, S. D., Zheng, W., Brink, T. G., et al. 2018, *ApJ*, 860, 90, doi: [10.3847/1538-4357/aac32c](https://doi.org/10.3847/1538-4357/aac32c)

Weaver, T. A., Zimmerman, G. B., & Woosley, S. E. 1978, *ApJ*, 225, 1021, doi: [10.1086/156569](https://doi.org/10.1086/156569)

Wheeler, J. C., Johnson, V., & Clocchiatti, A. 2015, *MNRAS*, 450, 1295, doi: [10.1093/mnras/stv650](https://doi.org/10.1093/mnras/stv650)

Wongwathanarat, A., Müller, E., & Janka, H. T. 2015, *A&A*, 577, A48, doi: [10.1051/0004-6361/201425025](https://doi.org/10.1051/0004-6361/201425025)

Woosley, S. E. 2019, *ApJ*, 878, 49, doi: [10.3847/1538-4357/ab1b41](https://doi.org/10.3847/1538-4357/ab1b41)

Woosley, S. E., & Bloom, J. S. 2006, *ARA&A*, 44, 507, doi: [10.1146/annurev.astro.43.072103.150558](https://doi.org/10.1146/annurev.astro.43.072103.150558)

Woosley, S. E., Heger, A., & Weaver, T. A. 2002, *Reviews of Modern Physics*, 74, 1015, doi: [10.1103/RevModPhys.74.1015](https://doi.org/10.1103/RevModPhys.74.1015)

Woosley, S. E., Langer, N., & Weaver, T. A. 1995, *ApJ*, 448, 315, doi: [10.1086/175963](https://doi.org/10.1086/175963)

Wygoda, N., Elbaz, Y., & Katz, B. 2019, *MNRAS*, 484, 3941, doi: [10.1093/mnras/stz145](https://doi.org/10.1093/mnras/stz145)

Xiang, D., Wang, X., Mo, J., et al. 2019, *ApJ*, 871, 176, doi: [10.3847/1538-4357/aaf8b0](https://doi.org/10.3847/1538-4357/aaf8b0)

Yoon, S.-C., Dessart, L., & Clocchiatti, A. 2017, *ApJ*, 840, 10, doi: [10.3847/1538-4357/aa6afe](https://doi.org/10.3847/1538-4357/aa6afe)

Yoon, S. C., Gräfener, G., Vink, J. S., Kozyreva, A., & Izzard, R. G. 2012, *A&A*, 544, L11, doi: [10.1051/0004-6361/201219790](https://doi.org/10.1051/0004-6361/201219790)

Yoon, S. C., Woosley, S. E., & Langer, N. 2010, *ApJ*, 725, 940, doi: [10.1088/0004-637X/725/1/940](https://doi.org/10.1088/0004-637X/725/1/940)

Yoshii, Y., Tomita, H., Kobayashi, Y., et al. 2003, *ApJ*, 592, 467, doi: [10.1086/375572](https://doi.org/10.1086/375572)

Zapartas, E., de Mink, S. E., Van Dyk, S. D., et al. 2017, *ApJ*, 842, 125, doi: [10.3847/1538-4357/aa7467](https://doi.org/10.3847/1538-4357/aa7467)